GLOBAL BIOGEOCHEMICAL CYCLES, VOL. 11, NO. 4, PAGES 535–560, DECEMBER 1997

The contribution of terrestrial sources and sinks to trends in the seasonal cycle of atmospheric carbon dioxide

James T. Randerson,[1,2] Matthew V. Thompson,[1,2,3] Thomas J. Conway,[4]
Inez Y. Fung,[5,6] and Christopher B. Field[1]

Abstract. We characterized decadal changes in the amplitude and shape of the seasonal cycle of atmospheric CO_2 with three kinds of analysis. First, we calculated the trends in the seasonal cycle of measured atmospheric CO_2 at observation stations in the National Oceanic and Atmospheric Administration Climate Monitoring and Diagnostic Laboratory network. Second, we assessed the impact of terrestrial ecosystems in various localities on the mean seasonal cycle of CO_2 at observation stations using the Carnegie-Ames-Stanford Approach terrestrial biosphere model and the Goddard Institute for Space Studies (GISS) atmospheric tracer transport model. Third, we used the GISS tracer model to quantify the contribution of terrestrial sources and sinks to trends in the seasonal cycle of atmospheric CO_2 for the period 1961-1990, specifically examining the effects of biomass burning, emissions from fossil fuel combustion, and regional increases in net primary production (NPP). Our analysis supports results from previous studies that indicate a significant positive increase in the amplitude of the seasonal cycle of CO_2 at Arctic and subarctic observation stations. For stations north of 55°N the amplitude increased at a mean rate of 0.66% yr^{-1} from 1981 to 1995. From the analysis of ecosystem impacts on the mean seasonal cycle we find that tundra, boreal forest, and other northern ecosystems are responsible for most of the seasonal variation in CO_2 at stations north of 55°N. The effects of tropical biomass burning on trends in the seasonal cycle are minimal at these stations, probably because of strong vertical convection in equatorial regions. From 1981 to 1990, fossil fuel emissions contributed a trend of 0.20% yr^{-1} to the seasonal cycle amplitude at Mauna Loa and less than 0.10% yr^{-1} at stations north of 55°N. To match the observed amplitude increases at Arctic and subarctic stations with NPP increases, we find that north of 30°N a 1.7 Pg C yr^{-1} terrestrial sink would be required. In contrast, over regions south of 30°N, even large NPP increases and accompanying terrestrial sinks would be insufficient to account for the increase in high-latitude amplitudes.

1. Introduction

The amplitude of the seasonal cycle of atmospheric CO_2 increased approximately 20% at the Mauna Loa observatory from 1958 to 1994 and approximately 40% at Point Barrow, Alaska, from 1961 to 1994 [*Keeling et al.*, 1996]. Arctic and subarctic CO_2 observation stations in the National Oceanic and Atmospheric Administration Climate Monitoring and Diagnostic Laboratory (NOAA/CMDL) flask network, including Alert, Cold Bay, Ocean Station M, and Mould Bay, show a similar trend during the 1980s [*Manning*, 1993; *Conway et al.*, 1994]. As the seasonal cycle of atmospheric CO_2 at surface observation stations in the northern hemisphere is driven primarily by net ecosystem production (NEP) fluxes from terrestrial ecosystems [*Tucker et al.*, 1986; *Fung et al.*, 1987; *Keeling et al.*, 1989a; *Knorr and Heimann*, 1995; *Erickson et al.*, 1996], the increase in the amplitude suggests that northern hemisphere terrestrial ecosystems are experiencing greater CO_2 uptake during the growing season and greater CO_2 release during periods outside the growing season.

In addition to NEP from terrestrial ecosystems, surface fluxes from fossil fuel combustion, biomass burning, and ocean exchange also contribute to the seasonal cycle of atmospheric CO_2. Systematic changes in the magnitude and seasonal distribution of these sources and sinks, as well as changes in atmospheric transport, may also drive trends in the seasonal cycle of CO_2.

Here we focus on both direct and indirect anthropogenic forcing of the seasonal cycle arising from long-term (decadal) changes in terrestrial surface fluxes. The two human activities that most directly influence the seasonal cycle of CO_2 are the consumption of fossil fuels and the burning of forests and grasslands. Fossil fuel emissions have increased from 2.6 Pg C/yr in 1960 to over 6 Pg C/yr in the 1990s [*Boden et al.*, 1995]. This increase in emissions (confined mostly to the

[1]Carnegie Institution of Washington, Department of Plant Biology, Stanford, California.
[2]Department of Biological Sciences, Stanford University, Stanford, California.
[3]Now at Department of Organismic and Evolutionary Biology, Harvard University, Cambridge, Massachusetts.
[4]Climate Monitoring and Diagnostics Laboratory, National Oceanic and Atmospheric Administration, Boulder, Colorado.
[5]NASA Goddard Institute for Space Studies, New York, New York.
[6]School of Earth and Ocean Sciences, University of Victoria, Victoria, British Columbia, Canada.

Copyright 1997 by the American Geophysical Union.

Paper number 97GB02268.
0886-6236/97/97GB-02268$12.00

northern hemisphere) has led to a strengthening of the meridional gradient of CO_2 with greater buildup in the northern hemisphere [*Keeling et al.*, 1989b]. Seasonal variation in atmospheric circulation leads to variable movement of this enriched northern hemisphere air across observation stations, inducing trends in the observed seasonal cycle [*Heimann et al.*, 1986]. The interaction of fossil fuel emissions with atmospheric transport is enhanced in many regions by seasonal variation in the rates of fossil fuel emission. In midlatitude and high-latitude regions, fossil fuel emissions are higher during winter months because of added demands for heating [*Rotty*, 1987]. Recent ^{14}C measurements suggest that, at least for northern Europe, fossil fuel emissions vary seasonally by a factor of 2 and that this seasonal variation in emissions contributes substantially to the observed seasonal cycle of CO_2 [*Levin et al.*, 1995].

In contrast to the relatively well documented record of fossil fuel emissions, much less is known about changes in the frequency and geographic extent of biomass burning over the last several decades. Biomass burning occurs predominately during the dry season in tropical regions [*Hao and Liu*, 1994; *Crutzen and Andreae*, 1990]. The strong seasonality of these fluxes and the seasonal movement of the Intertropical Convergence Zone (ITCZ) give them a large impact on tropospheric CO_2 in equatorial regions [*Iacobellis et al.*, 1994].

Human modification of terrestrial NEP can also induce trends in the seasonal cycle of CO_2. Because NEP is defined as the difference between heterotrophic respiration and net primary production (NPP), a change in the seasonal cycle of either of these one way fluxes, whether in phase, magnitude, or form, will alter the seasonal cycle of NEP [*Houghton*, 1987]. Changes in the seasonal cycle of respiration can lead to increases in the seasonal amplitude of atmospheric CO_2 through several different mechanisms. First, increases in winter temperature could shift respiration from summer to winter, leading to an increase in the seasonal amplitude [*Houghton*, 1987]. Model simulations designed to test this hypothesis [*Houghton*, 1987] suggest, however, that the observed winter warming is too small to explain the amplitude increases, given a realistic range of the response of respiration to temperature. Second, the expansion and intensification of agriculture and other anthropogenic disturbance in recent decades may lead to greater rates of decomposition of recently senesced plant material during fall and winter months, through changes in the structure and chemical composition of leaves and roots, thus driving an increase in the amplitude through a shift in the seasonal timing of heterotrophic respiration and NPP [*Kohlmaier et al.*, 1989; *Randerson et al.*, 1996].

Stimulation of NPP could also be driving increases in the amplitude. Increases in atmospheric CO_2 could be contributing to NPP increases, but the evidence to date indicates that CO_2 responses of NPP are unlikely to be the only or even the dominant driver [*Houghton*, 1987; *Kohlmaier et al.*, 1989]. CO_2 responses of NPP could explain all of the amplitude increases only if the sensitivity of NPP to CO_2 fertilization (often characterized by the β factor [*Amthor and Koch*, 1996]) far exceeds that measured in CO_2 enrichment studies. Other factors that may be stimulating NPP include fertilization from nitrogen deposition [*Townsend et al.*, 1996] and a lengthening of the growing season in high-latitude ecosystems in response to spring warming [*Keeling et al.*, 1996; *Myneni et al.*, 1997].

Here we present results from three complementary sets of analyses that address the impact of terrestrial surface fluxes on trends in the seasonal cycle. First, we assessed trends in the seasonal cycle of CO_2 from stations in the NOAA/CMDL flask network using an algorithm that is sensitive to changes in the amplitude and the shape of the seasonal cycle and data that extend through 1995. Second, we identified the contribution of individual terrestrial ecosystems to the mean seasonal cycle of CO_2 at observation stations. For this analysis we used the Goddard Institute for Space Studies (GISS) atmospheric tracer transport model [e.g., *Fung et al.*, 1991] to distribute steady state terrestrial NEP fluxes from the Carnegie-Ames-Stanford approach (CASA) model [*Potter et al.*, 1993]. This allowed us to characterize spatial "footprints" defined as the proportional contribution of seasonal variation in CO_2 concentrations at each measurement site due to surface exchange in each biome or region. Footprints are useful for attributing observed anomalies in the CO_2 record to interannual variation in ecosystem fluxes from specific regions. With the footprints we can ask, for example, whether the trend in the amplitude at Mauna Loa represents a change in vegetation dynamics over the entire northern hemisphere or just in boreal and tundra ecosystems.

In the third set of analyses we investigated effects on trends in the seasonal cycle from biomass burning, emissions from fossil fuel combustion, and NPP increases in terrestrial ecosystems. This investigation extends the work of *Kohlmaier et al.* [1989] by directly coupling multiyear NEP time series (generated by CASA [*Thompson et al.*, 1996]) to the GISS tracer model. The combination of the CASA and GISS model experiments performed here allowed us to quantify the magnitude and location of terrestrial NPP increases required to simultaneously account for both the observed trends in the seasonal cycle and reasonable global sums of terrestrial uptake.

2. Methods

Both the methods and results sections are divided into three sections: (1) analysis of trends in the seasonal cycle from stations in the NOAA/CMDL flask network, (2) analysis of the footprints of various biomes at observation stations obtained using monthly, steady state NEP fluxes from CASA and the GISS atmospheric tracer model, and (3) modeled impacts of anthropogenic forcing on trends in the seasonal cycle of atmospheric CO_2.

2.1. Trends in the Seasonal Cycle at Stations in the NOAA/CMDL Flask Network

We used monthly mean CO_2 concentrations from the NOAA/CMDL flask network to calculate trends in the seasonal cycle. The monthly mean NOAA/CMDL data product is obtained from a combination of curve fitting and digital filtering of the weekly flask data [*Thoning et al.*, 1989]. As our focus here is on decadal scale changes, we considered only

Table 1. NOAA/CMDL Flask Station Amplitudes

	Station	Abbreviation	Latitude, °N	Longitude, °W	Elevation, m	Time Period	Span, months	Amplitude, ppm	Amplitude Trend, % yr^{-1}[a]	F_s[b]	*df*
1	Alert, NWT, Canada	ALT	82 27'	62 31'	210	June 1985 to Nov. 1995	126	14.29	1.52	8.77**	17
2	Mould Bay, Canada	MBC	76 14'	119 20'	15	April 1980 to Nov. 1995	188	14.10	1.33	25.30***	28
3	Point Barrow, Alaska	BRW	71 19'	156 36'	11	May 1971 to Dec. 1995	296	15.15	0.45	5.13*	46
4	Ocean Station M	STM	66 00'	-2 00'	6	March 1981 to Oct. 1995	176	14.24	0.63	3.87	26
5	Cold Bay, Alaska	CBA	55 12'	162 43'	25	Oct. 1978 to Dec. 1995	207	15.77	0.50	1.53	30
6	Shemya Island, Alaska	SHM	52 43'	174 06'	40	Sep. 1985 to Dec. 1995	124	17.76	-1.38	3.49	16
7	Cape Meares, Oregon	CMO	45 29'	124 00'	30	March 1982 to May 1995	159	10.24	-0.36	0.29	36
8	Niwot Ridge, Colorado	NWR	40 03'	105 38'	3749	Jan. 1976 to Dec. 1995	240	8.02	-0.99	1.10	23
9	Sand Island, Midway	MID	28 13'	177 22'	4	May 1985 to Dec. 1995	128	8.79	0.48	0.34	18
10	Key Biscayne, Florida	KEY	24 40'	80 12'	3	April 1976 to Nov. 1995	236	7.62	0.45	0.83	36
11	Mauna Loa, Hawaii	MLO	19 32'	155 35'	3397	July 1976 to Dec. 1995	234	6.49	0.69	6.80*	35
12	Kumukahi, Hawaii	KUM	19 31'	154 49'	3	March 1980 to Nov. 1995	189	8.21	0.03	0.01	27
13	Mariana Island, Guam	GMI	13 26'	-144 47'	2	March 1979 to Dec. 1995	202	6.29	1.16	2.47	30
14	Christmas Island	CHR	2 00'	157 19'	3	March 1984 to July 1994	125	2.96	-2.06	1.50	17
15	Mahe Island, Seychelles	SEY	-4 40'	-55 10'	3	Jan. 1986 to Dec. 1995	120	2.57	9.54	9.21**	16
16	Ascension Island	ASC	-7 55'	14 25'	54	Aug. 1979 to Dec. 1995	197	1.60	4.60	7.48*	29
17	Matatula Point, Samoa	SMO	-14 15'	170 34'	30	Aug. 1973 to Dec. 1995	269	0.57	7.47	7.35**	41
18	Cape Grim, Tasmania	CGO	-40 41'	-144 41'	94	April 1984 to Oct. 1995	139	0.94	-1.15	0.28	20
19	South Pole	SPO	-89 59'	24 48'	2810	July 1975 to Oct. 1995	244	1.17	-1.62	6.89*	37

[a]Amplitude trends (T_{amp}) were calculated according to the procedure described in section 2.1. Amplitude trends are linear over the span indicated.
[b]F_s is the *F* distribution number [*Sokal and Rohlf*, 1980]. The asterisks denote the significance of the *F* test described in section 2.1: * = $0.05 \geq p > 0.01$, ** = $0.01 \geq p > 0.001$, and *** = $p \leq 0.001$. The degrees of freedom for the *F* test are given in a separate column, denoted by *df*.

stations for which 10 years of continuous data were available. A total of 19 stations met this criterion (Table 1).

The secular increase in CO_2 (driven by fossil fuel combustion, deforestation, and terrestrial and oceanic sources and sinks) was removed from the time series at each station through the use of a seasonal trend decomposition procedure based on locally weighted regressions (STL) [*Cleveland et al.*, 1990]. The STL procedure split each time series into three components consisting of a low-frequency trend, a seasonal cycle, and a residual. Following *Manning* [1993], we used a smoothing window of 5 years with the STL procedure to remove the secular (low-frequency) trend. Trends in the amplitude of the seasonal cycle were calculated by using the sum of the seasonal cycle and residual components of the time series (hereafter referred to as the detrended time series) following the procedure described below.

First, a mean seasonal cycle of the detrended time series was constructed for each station by separately averaging all available data for each month (i.e., the mean seasonal cycle consisted of the average of all January points, the average of all February points, and so on.). The interannual growth rate b was separately calculated for each month of each detrended time series as the slope of a linear regression of CO_2 versus year. The trend in the amplitude (T_{amp}, Table 1) was derived from the mean seasonal cycle and the interannual growth rates:

$$T_{amp} = \left(\frac{b_{max} - b_{min}}{C_{max} - C_{min}} \right) 100, \quad (1)$$

where b_{max} is the interannual growth rate during the month of maximum CO_2 concentration (from the mean seasonal cycle), b_{min} is the interannual growth rate during the month of minimum CO_2 concentration (from the mean seasonal cycle), and C_{max} and C_{min} are the corresponding maximum and minimum monthly CO_2 concentrations from the mean seasonal cycle. Changes in CO_2 during months of maximum and minimum CO_2 concentration lead to changes in the peak-to-trough amplitude of the seasonal cycle. The units of T_{amp} are percent per year.

The significance of T_{amp} was assessed by comparing b_{max} and b_{min}. Because b_{max} and b_{min} are slopes of linear regressions of CO_2 versus time, we performed an *F* test for the difference between two regression slopes as described in box 14.8 of *Sokal and Rohlf* [1980]. We report values of T_{amp} for which b_{max} and b_{min} were significantly different ($p \leq 0.05$) with asterisks in Table 1. The filtering and detrending processes used here requires that some caution be taken in interpreting these statistical tests.

The pattern of seasonal variation in CO_2 interannual growth rates and T_{amp} was also calculated for groups of stations with the idea that by pooling data from geographically related sites it would be possible to improve the confidence level of trend estimates [*Manning*, 1993]. The same procedure as described above was followed. Our estimate for the slope b and its standard deviation accounted for the multiple CO_2 measurements (one from each station in the pool) that comprised each month of the combined time series (section 14.8 of *Sokal and Rohlf* [1980]).

This procedure for calculating the trends in the seasonal cycle builds on previous studies [*Conway et al.*, 1994; *Manning*, 1993; *Chan and Wong*, 1990; *Cleveland et al.*, 1983; *Pearman and Hyson*, 1981]. The procedure does not assume that shape of the seasonal cycle remains constant through time: the CO_2 interannual growth rate for each month is calculated independently of other months. Thus it is possible to evaluate changes in the shape of the seasonal cycle, not just its amplitude. For example, it is possible to compare the contribution of different potential forcing functions (e.g., CO_2 fertilization, fossil fuel combustion, and biomass burning) to the observed seasonal pattern of CO_2 growth rates. This approach does, however, limit the interpretation to linear trends over the entire time series; year-to-year variation in the amplitude cannot be determined from this method. At some monitoring stations such as Point

Barrow, year-to-year variation in amplitude growth appears to be substantial and is correlated with temperature variability [*Keeling et al.*, 1996]. Thus techniques that allow the calculation of year-to-year changes in the amplitude may provide unique insight into controls on interannual variability in the carbon cycle that complements the approach taken here.

Keeling et al. [1996] demonstrate advances in the time of the downward 0 ppm crossing of the detrended seasonal cycle at Barrow and Mauna Loa. For these two stations the downward zero crossing advanced approximately 7 days from the early 1960s to 1994 (approximately 2-3 days per decade), although most of this advance occurred after the mid-1970s. We estimated changes in the downward 0 ppm crossing time using the mean seasonal cycle and the interannual growth rates described above. The Julian day of the 0 ppm crossing was found by determining the intercept of the two points spanning the 0 ppm crossing. The interannual CO_2 growth rates were then added to the mean seasonal cycle of CO_2, and the calculation was repeated. The sum of the mean seasonal cycle and the interannual CO_2 growth rates describes how the seasonal cycle would appear after 1 year, given the observed month-to-month variation in interannual CO_2 growth rates. The difference between the two estimates of the 0 ppm crossing time was then multiplied by a factor of 10 and expressed as a shift in days of year per decade.

2.2. Footprints of Terrestrial Ecosystems at Observation Stations

2.2.1. 1990 steady state NEP fluxes from the CASA model. We used the CASA biosphere model [*Potter et al.*, 1993] to produce monthly NPP fluxes (Table 2) representing 1990 for the footprint analysis (section 2.2.3) and also as a target for the NPP stimulation runs (section 2.3.3). For the footprint analysis, NPP fluxes from CASA were used to drive the heterotrophic submodel of CASA for 5000 years (60,000 monthly time steps) to obtain steady state plant, litter, and soil carbon pool sizes and NEP fluxes.

Growing season net flux (GSNF), defined as the annual sum of monthly NEP fluxes during months when an ecosystem is a net sink of atmospheric CO_2 [*Fung et al.*, 1983], is a useful indicator of the seasonality in the net exchange of CO_2 between terrestrial ecosystems and the atmosphere. At steady state, GSNF is zero where NPP and heterotrophic respiration are perfectly in phase. It is large where NPP and heterotrophic respiration occur at very different times of the year and NPP is large. The global sum of GSNF from our steady state model run (13.6 Pg C yr^{-1}) is similar to the sum derived in experiment 3 of *Fung et al.* [1983] (13.0 Pg C yr^{-1}). The regional distribution of this flux, however, is quite different. CASA predicts strongly seasonal NEP in tropical regions, driven by seasonal changes in soil moisture and canopy leaf area (Table 2). In the boreal forest regions of the northern hemisphere, annual NPP from CASA is approximately a third less than estimates used by *Fung et al.* [1983] and *Fung et al.* [1987]. As a consequence, the CASA GSNF for boreal forests is substantially lower than that of *Fung et al.* [1983, 1987].

Table 2. 1990 Steady State CASA Fluxes

Class	Vegetation Type[a]	Area, 10^6 km^2	NPP, g C m^{-2} yr^{-1}	GSNF, g C m^{-2} yr^{-1}
1	tropical rainforests	13.45	1085	142
2	broadleaf deciduous trees	3.30	508	135
3	broadleaf and needleleaf trees	6.60	552	158
4	needleleaf evergreen trees	12.97	276	104
5	needleleaf deciduous trees	5.75	290	128
6	savannas	21.74	748	159
7	perennial grasslands	8.95	264	84
8	broadleaf shrubs with bare soil	11.01	89	24
9	tundra	7.08	112	59
10	Desert	16.89	21	6
11	cultivation	24.81	363	127
	global sum:	132.60	54.9×10^{15}	13.6×10^{15}

[a]Land cover classification from *Defries and Townshend* [1994]. See text for definition of terms.

Monthly NPP in CASA is calculated as the product of absorbed photosynthetically active radiation by plant canopies (APAR) and a spatially varying light use efficiency [*Field et al.*, 1995]. The flow of carbon through plant, litter, and soil organic matter pools is incremented at a monthly time step. The turnover of times of living biomass (leaves, fine roots, and woody biomass) are separately prescribed for each vegetation type [*Thompson et al.*, 1996]. The seasonal flow of organic matter from plants to heterotrophs (e.g., litterfall, root mortality, and coarse woody debris) depends on the seasonal course of satellite-derived leaf area index (LAI) [*Randerson et al.*, 1996]. Maximum first-order rate constants for the turnover of litter and soil pools at 30°C were taken from *Parton et al.* [1993]. The response of heterotrophic respiration to surface air temperature is described by using a Q10 function of 1.5 [*Raich and Potter*, 1995; *Knorr and Heimann*, 1995]. The response of heterotrophic respiration to soil moisture is a function of stored soil water, estimated evapotranspiration and potential evapotranspiration (for specific details on rates of litter decomposition and on soil moisture controls, see *Randerson et al.* [1996]).

Inputs to CASA included a 1990 monthly normalized difference vegetation index (NDVI) product derived from the NOAA/NASA Pathfinder data set (described below), surface solar insolation [*Bishop and Rossow*, 1991], mean temperature and precipitation from the period 1950 to 1980 [*Shea*, 1986], soil texture [*Zobler*, 1986] and a land cover classification based on NDVI [*DeFries and Townshend*, 1994].

To estimate the monthly fraction of photosynthetically active radiation intercepted by plant canopies (FPAR), we used the mean of the three Pathfinder 10-day maximum composite NDVI images available for each month in 1990. We did not use one of the NDVI products with a monthly maximum composite (e.g., the Fourier adjusted, solar zenith angle corrected, interpolated and reconstructed (FASIR) product described by *Sellers et al.* [1994] or the Pathfinder monthly data set) because of the distortion of the seasonal cycle that results from the maximum compositing procedure. Specifically, maximum compositing artificially increases the width of the growing season by overestimating NDVI during the early phases of canopy development and also during periods of leaf senescence [*Los et al.*, 1994]. The distortion is greatest in ecosystems at high latitudes where the growing season is short (Figure 1). While the 10-day maximum

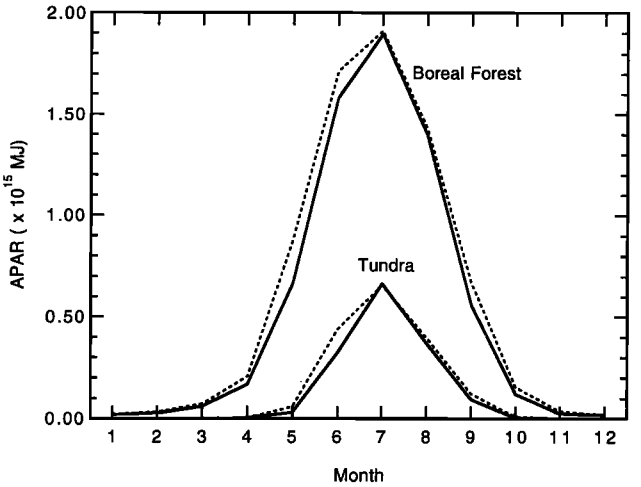

Figure 1. Monthly APAR as calculated using the average of the three Pathfinder 10 day maximum composite NDVI images used here (solid line) and the Pathfinder monthly maximum composite NDVI images (dotted line). For purposes of comparison, the Pathfinder monthly maximum composite product was adjusted by a constant factor so that during the month of peak absorption it yielded the same APAR value as the product derived from the 10 day composites. The maximum compositing technique overestimates APAR in the spring and to a lesser extent during the fall. Over the course of one year, APAR estimated from the monthly composites is 10.2% greater than APAR estimated from the average of the three 10 day composites for the sum of boreal forests and tundra (8.84 x 10^{15} MJ PAR vs. 8.02 x 10^{15} MJ PAR).

composites used here also share this bias, there is less distortion than there is in the monthly product because the sampling period is smaller. The smaller sampling period may mean, however, that our NDVI product suffers from more cloud contamination than the monthly maximum composited NDVI products.

2.2.2. GISS atmospheric tracer transport model. In the model experiments presented here, we used the three-dimensional GISS coarse resolution atmospheric tracer transport model [*Fung et al.*, 1983,1991; *Russell and Lerner*, 1981]. The tracer model has an 8° x 10° grid cell resolution and nine vertical layers. The circulation statistics of the coarse resolution tracer model are the same as those of the 4°x 5° model [e.g., *Tans et al.*, 1990; *Fung et al.*, 1987] from which it was derived. The model includes a horizontal diffusion scheme for deep convective events that yields realistic interhemispheric exchange times [*Prather et al.*, 1987]. In the CO_2 Transport Comparison Project the interhemispheric exchange times estimated by the coarse resolution GISS model are near the center of the broad range of values obtained from other tracer models [*Law et al.*, 1996 Table 3].

For each set of monthly surface fluxes, or tracer, in the footprint analysis we ran the GISS tracer model for 3 years to achieve steady state concentrations of atmospheric CO_2 at the surface. In following sections (2.3.2 and 2.3.3) we describe transient flux experiments that required continuous 33 year tracer model runs (3 years to achieve steady state and 30 years from 1961 to 1990 to allow analysis of trends in the modeled concentration data). The version of the GISS tracer model used in these experiments accepts a new set of surface fluxes each year while recycling the same set of GCM winds. As such, there is no interannual variation in transport.

2.2.3. Description of tracers and methodology in the footprint analysis. We assessed the contribution of different biomes to the seasonal cycle of CO_2 at the observation stations by coupling 1990 steady state NEP fluxes from the CASA terrestrial biosphere model to the GISS atmospheric tracer transport model. Hereafter, we refer to the "footprint" of an observation station as the geographic domain from which surface fluxes influence the measured seasonal variation in gas concentration. Since we sought to identify the steady state contribution of different biomes within the terrestrial biosphere to the seasonal cycle of CO_2, in one analysis we excluded biomass burning, ocean, and fossil fuel tracers. For this analysis we performed three sets of tracer model runs, partitioning monthly NEP by biome, latitude, and intensity of agricultural use (Table 3, Figure 2). In a second analysis we included biomass burning, fossil fuel, and ocean tracers along with a tracer consisting of NEP fluxes from all terrestrial biomes.

In the analysis of the contribution of individual biomes, *DeFries and Townshend* [1994] vegetation classes were used to group CASA NEP fluxes into 10 tracers from tundra at high latitudes in the northern hemisphere (tracer 1.1 in Table 3 and Figure 2a) to forests, shrubs, and deserts in the southern hemisphere (tracer 1.10 in Table 3 and Figure 2a). In the analysis of the contribution of various latitudinal bands we partitioned NEP fluxes into the following five regions: (1) north of 60°N, (2) 50°N to 60°N, (3) 40°N to 50°N, (4) 30°N to 40°N, and (5) south of 30°N (Figure 2b). An agricultural tracer was constructed from the product of a map of fractional agriculture cover [*Matthews*, 1983] and monthly maps of CASA NEP fluxes (Figure 2c). Each grid cell in the map of fractional agricultural cover was assigned a value of 1.0, 0.75, 0.50, 0.2, or 0.0 based on the intensity of land use from Table 1 of *Matthews* [1983].

To calculate the overall contribution of biogenic surface fluxes (NEP) to the seasonal cycle of CO_2, a separate footprint analysis was performed that included four tracers: steady state NEP fluxes from CASA (section 2.2.1), 1990 fossil fuel emissions (section 2.3.2), 1990 biomass burning (section 2.3.1), and ocean exchange [*Tans et al.*, 1990]. The ocean fluxes were constructed as described in the text (equations (1) and (2)) and footnotes of *Tans et al.* [1990]. Seasonal and geographic variation in the ocean carbon fluxes used here are summarized by Table 2 of *Tans et al.* [1990]. The peak-to-trough amplitude of the estimated seasonal cycle and its correlation with detrended NOAA/CMDL observations for the sum of all four tracers provide an indication of how well our model estimates agree with the observations.

The fractional contribution of each tracer i to the seasonal cycle of CO_2 at each observation station k is given by

$$F_k(i) = \frac{\sum_{t=1}^{12} |C_k(i,t)|}{\sum_{j=1}^{n} \left(\sum_{t=1}^{12} |C_k(j,t)| \right)}, \quad (2)$$

where $C_k(i,t)$ is the detrended concentration of CO_2 obtained

Table 3. Tracer Characteristics Used in the Footprint Analysis

Tracer	Vegetation Type	Location	Area, x 10^{12} m^2	NPP, Pg C yr^{-1}	GSNF, Pg C yr^{-1}
1.1	tundra	north of 50°N	7.38	0.80	0.42
1.2	boreal forest	40°N to 72°N	18.83	5.20	2.08
1.3	deciduous and mixed conifer forest	25°N to 65°N	7.39	3.82	1.15
1.4	agriculture, grassland, open woodland	70°N to 40°N	12.41	4.40	1.62
1.5	agriculture, grassland, open woodland	20°N to 40°N	13.67	4.97	1.52
1.6	agriculture, grassland, savanna	0°N to 20°N	10.54	5.72	1.47
1.7	shrubland, deserts	5°N to 50°N	20.97	0.65	0.20
1.8	tropical forest	25°N to 20°S	14.26	14.98	2.01
1.9	agriculture, grassland, savanna	0°S to 60°S	18.87	12.54	2.74
1.10	forests, shrublands and deserts	0°S to 60°S	8.43	1.82	0.41
2.1	all biomes	north of 60°N	14.82	2.37	1.12
2.2	all biomes	50°N to 60°N	14.53	4.83	1.88
2.3	all biomes	40°N to 50°N	16.04	5.70	1.99
2.4	all biomes	30°N to 40°N	15.59	4.15	1.24
2.5	all biomes	south of 30°N	71.58	37.84	7.39
3.1	agriculture	90°N to 90°S	17.45	8.49	2.49
3.2	no agriculture	90°N to 90°S	115.15	46.41	11.13
	global sum:		132.60	54.90	13.60

from the GISS model for tracer i at month t and at observation station k. Here, n is the total number of tracers in the footprint analysis. $F_k(i)$ reflects both the magnitude and the seasonal variation of surface fluxes (summarized in terrestrial ecosystems by GSNF) as well as the effects of atmospheric circulation.

Equation (2) includes no phase information: a particular tracer could have a high value of $F_k(i)$ even though its contribution caused a decrease in the amplitude of the seasonal cycle. To provide an index of agreement in phase for each tracer, we calculated the product-moment (Pearson) correlation coefficient (section 15.2 of *Sokal and Rohlf* [1980]) between each tracer i and the observed seasonal cycle at each station k.

$$R_k(i) = \frac{\sum_{t=1}^{12} C_{obs,k}(t) C_k(i,t)}{\sqrt{\sum_{t=1}^{12} \left(C_{obs,k}(t)\right)^2 \sum_{t=1}^{12} \left(C_k(i,t)\right)^2}}, \quad (3)$$

where $C_{obs,k}(t)$ is the detrended monthly mean CO_2 concentration from the NOAA/CMDL flask network for station k, as described in section 2.1, and $C_k(i,t)$ is the detrended monthly mean CO_2 concentrations from the GISS tracer model for tracer i. $R_k(i)$ equals 1.0 when a tracer signal is perfectly in phase with the observed seasonal cycle and -1.0 when a tracer signal is perfectly out of phase.

2.3. Impacts of Anthropogenic Forcing on Trends in the Seasonal Cycle

2.3.1. Biomass burning. We used monthly 5° x 5° tropical biomass burning estimates for North and South America, Africa, and Asia developed by W. M. Hao [*Hao and Liu*, 1994; *Hao et al.*, 1990]. Deforestation, shifting cultivation, and savanna fire components of biomass burning were confined to the dry season [*Hao and Liu*, 1994]. Fuel wood and agricultural residue burning was assumed to occur uniformly throughout the year [*Hao and Liu*, 1994]. The database is representative of the late 1970s. To obtain a global estimate appropriate for 1990, we multiplied the Hao estimates at each cell by a constant scalar so that the global annual sum was 3.0 Pg C yr^{-1}. This total is greater than the 2.6 Pg C yr^{-1} value used by *Hunt et al.* [1996] for the period of the late 1980s but is within the 1.8-4.7 Pg C yr^{-1} range given by *Crutzen and Andreae* [1990].

The sum of carbon lost through biomass burning and related disturbance is balanced by regrowth to yield a net tropical source of approximately 1.6 Pg C yr^{-1} for the 1980s [*Schimel et al.*, 1995]. To account for this imbalance, it would be strictly necessary to reduce the flow of carbon to heterotrophic respiration in the CASA model. We did not make this correction, however, because it is likely to have only a minor impact on the seasonal cycle of tropical NEP and consequently the seasonal cycle of atmospheric CO_2 [*Hunt et al.*, 1996; *Iacobellis et al.*, 1994]. Specifically, in steady state tropical forests and savannas have an NPP of 30 Pg C yr^{-1} (Table 2). Changing heterotrophic respiration from 30 to 28.6 Pg C yr^{-1} (less than a 5% decrease in heterotrophic respiration) to account for this net source would only slightly alter the seasonal cycle of NEP in tropical regions.

The 1990 biomass burning tracer was used to drive the GISS transport model for 3 years. The contribution from biomass burning to the trend in the amplitude of the seasonal cycle at each station was determined by adding a mean seasonal cycle of CO_2 concentrations derived from either model estimates or NOAA/CMDL observations. The modeled seasonal cycle consisted of CO_2 concentrations obtained from the GISS tracer model driven by ocean exchange [*Tans et al.*, 1990], 1990 fossil fuel emissions (section 2.3.2), and steady state NEP fluxes from CASA (section 2.2.1). The trend in the amplitude (T_{amp}) due to changes in biomass burning was estimated for the 1971-1990 period by assuming that biomass burning

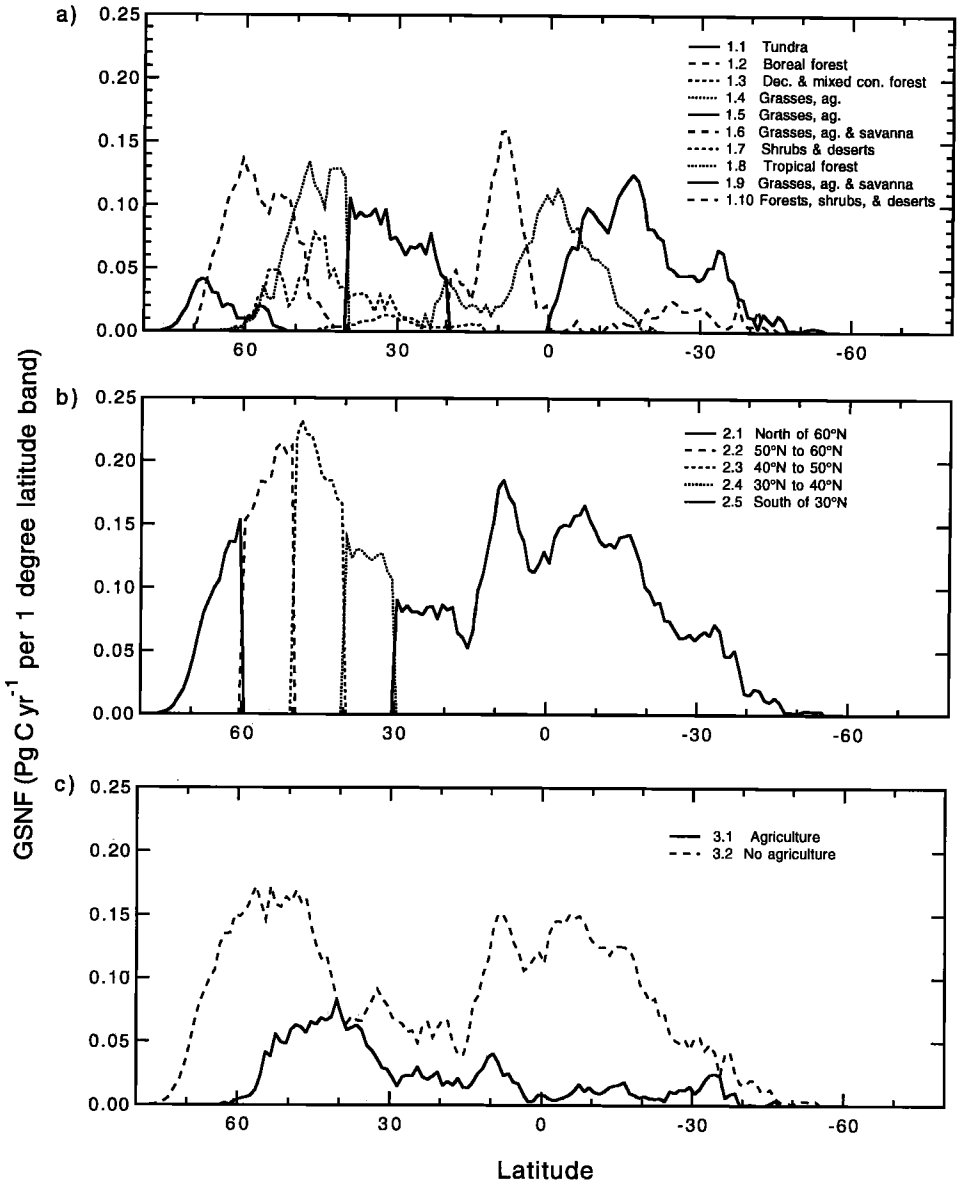

Figure 2. Latitudinal distribution of growing season net flux (GSNF) for biomes identified in the footprint analysis. Terrestrial steady state NEP fluxes from the CASA model were divided by (a) biome, (b) latitude band, and (c) agricultural use. Characteristics of each tracer are given in Table 3.

increased (with the same spatial distribution) from 1.0 Pg C yr^{-1} in 1971 to 3.0 Pg C yr^{-1} in 1990. A 2.0 Pg C yr^{-1} increase in the rate of biomass burning from 1971 to 1990 is consistent with rapid increases in the rate of deforestation observed in some tropical regions [e.g., *Houghton and Hackler*, 1994]. This estimate is preliminary, however, and serves only as a starting point for identifying the impact of biomass burning on observed trends.

2.3.2. Fossil fuel emissions. We constructed a continuous monthly time series of the spatial distribution of fossil fuel emissions from the period 1958 to 1990. Four 1° x 1° maps of annual fossil fuel combustion for 1960, 1970, 1980, and 1990 from the work of *Andres et al.* [1996] constrained the time series at decade intervals (Figures 3a and 3b). For years in between, interannual variation at each grid cell followed a scaled version of the trajectory of global fossil fuel emissions from the work of *Boden et al.* [1995] (Figure 3c). Smoothed monthly estimates were obtained by fitting a cubic spline through the annual sums [*Press et al.*, 1988].

Following *Heimann and Keeling* [1989], we superimposed a seasonal cycle on the smoothed monthly time series of fossil fuel emissions. Specifically, we used the GISS political geography map [*Lerner et al.*, 1988] to project the monthly fractional estimates of 1982 fossil fuel emissions contained in Table 5 of *Rotty* [1987] onto 12 monthly 1° x 1° maps (Figure 4). Areas outside the six regions identified by *Rotty* [1987] were assigned an invariant monthly emissions pattern.

The complete fossil fuel emission time series from 1958 to 1990 was then run through the GISS tracer model (2.2.2). To estimate T_{amp} induced by fossil fuel emissions at each station,

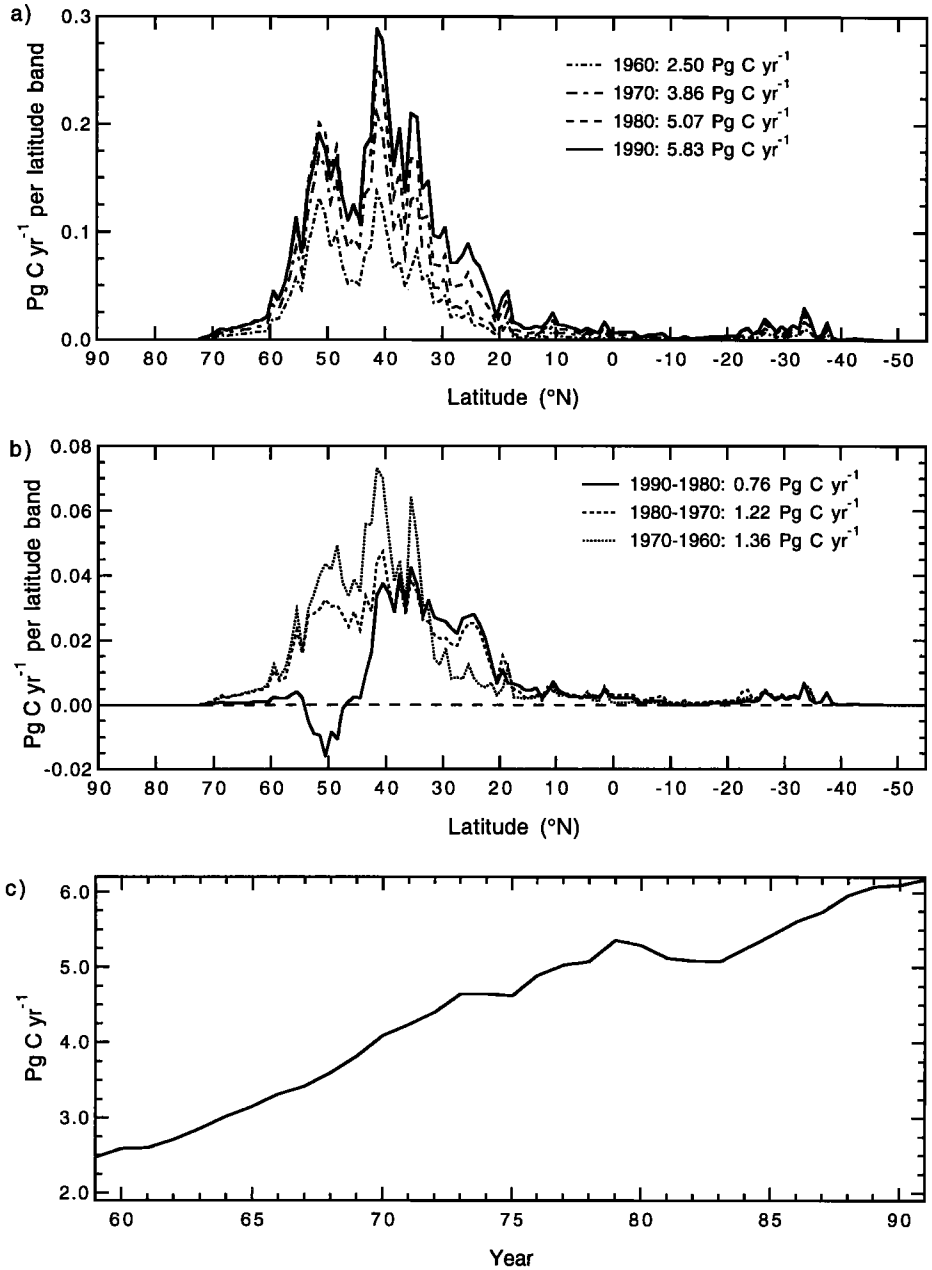

Figure 3. (a) Latitude distribution of annual emissions of the four 1° x 1° fossil fuel maps described by *Andres et al.* [1996]. Annual global sums for each of the four maps are presented next to the figure legend. (b) Difference in emission rates between each consecutive distribution for 1° latitude bands. The annual global sums of the differences are presented next to the figure legend. (c) History of global annual fossil fuel emissions from the work of *Boden et al.* [1995].

we first added a mean seasonal cycle of atmospheric CO_2 concentrations derived from either model estimates or NOAA/CMDL observations. The modeled seasonal cycle consisted of CO_2 concentrations obtained from the GISS tracer model driven by ocean fluxes [*Tans et al.*, 1990], 1990 biomass burning fluxes (section 2.3.1), and steady state NEP fluxes from CASA (section 2.2.1). We removed the secular (low-frequency) trend from the time series, using the STL procedure described in section 2.1. We estimated T_{amp} for the periods of 1961 to 1990, 1971 to 1990, and 1981 to 1990. The latter two sampling periods were included to allow comparisons with observation stations that became active during these periods.

2.3.3. NPP stimulation. Given the strong link between changes in NPP and the terrestrial carbon sink, as well as obvious impacts that changes in NPP may have on the seasonal cycle of atmospheric CO_2, we addressed two questions: (1) How much of an increase in global NPP using the coupled CASA-GISS model would be necessary to reproduce the increases in the amplitude of the seasonal cycle at high

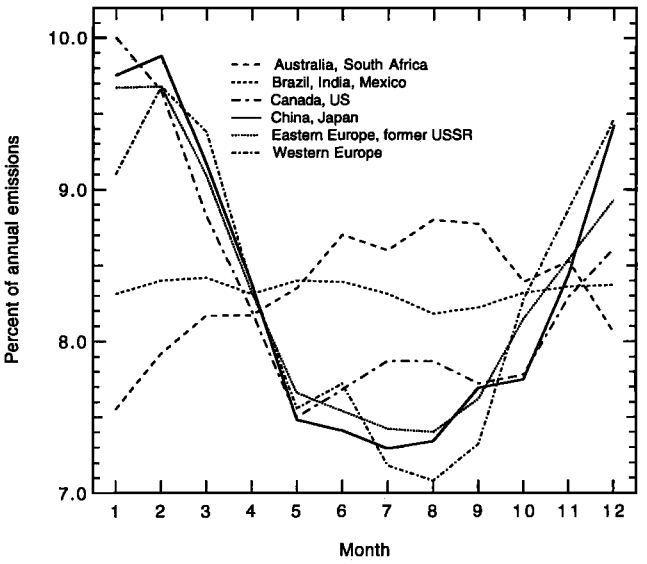

Figure 4. Monthly percentages of fossil fuel emissions for six major industrial regions for 1982 (from Table 5 of *Rotty* [1987]).

latitudes? (2) Would it be possible to reproduce the high-latitude amplitude increases and also obtain a realistic global sum for the terrestrial carbon sink?

To answer these questions, we executed a set of basic "building-block" CASA model runs which determined the fractional extent to which global NPP would have to increase in order to match multiples of a well-known estimate of the historical terrestrial carbon sink [*Houghton*, 1995] as in the work of*Thompson et al.* [1996]. Using spatial combinations of the NEP data derived from these runs to drive the GISS tracer transport model, we attempted to determine in what parts of the world an increase in NPP could both satisfy the large changes in the seasonal cycle of CO_2 observed at high-latitude stations and maintain carbon sequestration rates compatible with recent estimates. In the following paragraphs the five CASA-GISS model runs that we performed to address the first question (experiment 1) and the eight additional GISS tracer model runs that we performed to address the second question (experiment 2) are described in more detail.

For the five CASA model runs that served as a basis for this exercise it was necessary to specify both a history of annual NPP increase and a seasonal distribution. Following *Thompson et al.* [1996], in four model runs we increased annual NPP at each pixel by the fractional amount necessary to bring the global carbon sink in line with multiples of (1x, 2x, 3x, and 4x) the *Houghton* [1995] estimate (Figure 5). A second constraint for each of these four CASA runs was that in 1990 the spatial distribution of NPP had to match exactly the estimates of NPP described in section 2.2.1.

An iterative process was required to find a solution to these two constraints. NPP and carbon pool sizes obtained from the 5000 year steady state run described in section 2.2.1 were used to initialize a 300 year model run in which NPP remained constant, but heterotrophic respiration was allowed to vary in response to random temperature and precipitation anomalies taken from the data sets developed by *Hansen and Lebedeff* [1987, 1988] and *Baker et al.* [1995]. This was done to allow soil carbon pool sizes to equilibrate with a varying climate. With carbon pool sizes set from the 300 year run the first step in the iteration was to run CASA forward from 1880 to 1990, so that it matched the time history of the historical carbon sink. NPP in 1880 was initialized to the target NPP for 1990 from section 2.2.1. As a result of this initialization, at the end of the run in 1990, NPP was much higher than the target. In successive runs, initial NPP and carbon pool sizes in 1880 were scaled back at all grid cells by the following factor:

$$F = \left(1 - \frac{\mathrm{NPP}(1990) - \mathrm{NPP}_{\mathrm{target}}(1990)}{\mathrm{NPP}_{\mathrm{target}}(1990)}\right) \quad (4)$$

where NPP(1990) is global annual NPP from the most recent model run and $\mathrm{NPP}_{\mathrm{target}}(1990)$ is global annual NPP from the distribution described in section 2.2.1. The convergence criterion was that F had to be less than 1 in 10^{-4} parts from 1.0. In a fifth CASA model run, NPP was held constant from 1880 to 1990.

For each of the five CASA model runs, monthly gridded temperature anomalies [*Hansen and Lebedeff*, 1987, 1988] and monthly gridded precipitation anomalies [*Baker et al.*, 1995] from 1880 to 1990 were added to climatological means [*Shea*, 1986] to allow heterotrophic respiration to vary in response to climate. We did not have climate variation directly impact NPP because climate variability influences both heterotrophic respiration and the *Houghton* [1995] sink estimate. Because we calculate NPP as the difference between the sink and heterotrophic respiration, it would have been redundant to also explicitly consider climate variability effects on NPP. The spatial pattern of year-to-year variation in NPP is artificially uniform, however, because the historical sink estimate consists of a time series of global sums.

Monthly NEP from 1958 to 1990 from each of the five CASA model runs that comprised experiment 1 were run through the GISS tracer transport model. As in the fossil fuel analysis the first 3 years (1958, 1959, and 1960) were included to allow the GISS tracer model to reach a steady state before the analysis of surface concentrations began in 1961. Prior to estimating T_{amp} a modeled seasonal cycle of CO_2 derived from ocean exchange [*Tans et al.*, 1990], 1990 biomass burning (section 2.3.1), and 1990 fossil fuel emissions (section 2.3.2) was added to the CO_2 concentrations obtained from each of the five CASA simulations. The secular (low-frequency) trend was removed from the sum of the modeled CO_2 concentrations by using the STL procedure described in section 2.1. Estimates of T_{amp} from NPP stimulation were obtained by equation (1) for the periods from 1961 to 1990, from 1971 to 1990, and from 1981 to 1990.

In experiment 2, we made a series of additional GISS tracer model runs using surface fluxes that consisted of a spatial combination NEP from the constant NPP run and NPP stimulation run in which NEP matched the 3.0 multiple of the *Houghton* [1995] sink estimate (hereafter referred to as 3 x *Ho* following the naming convention of *Thompson et al.* [1996]). Using regional sections (or partitions) of NEP from the 3 x *Ho* run was an easy way to examine the effect of regional NPP increases on the meridional distribution of amplitude trends. We chose the 3 x *Ho* run (over the 1, 2, or 4 x *Ho* run) for this analysis because in experiment 1 the 3 x *Ho* run most closely

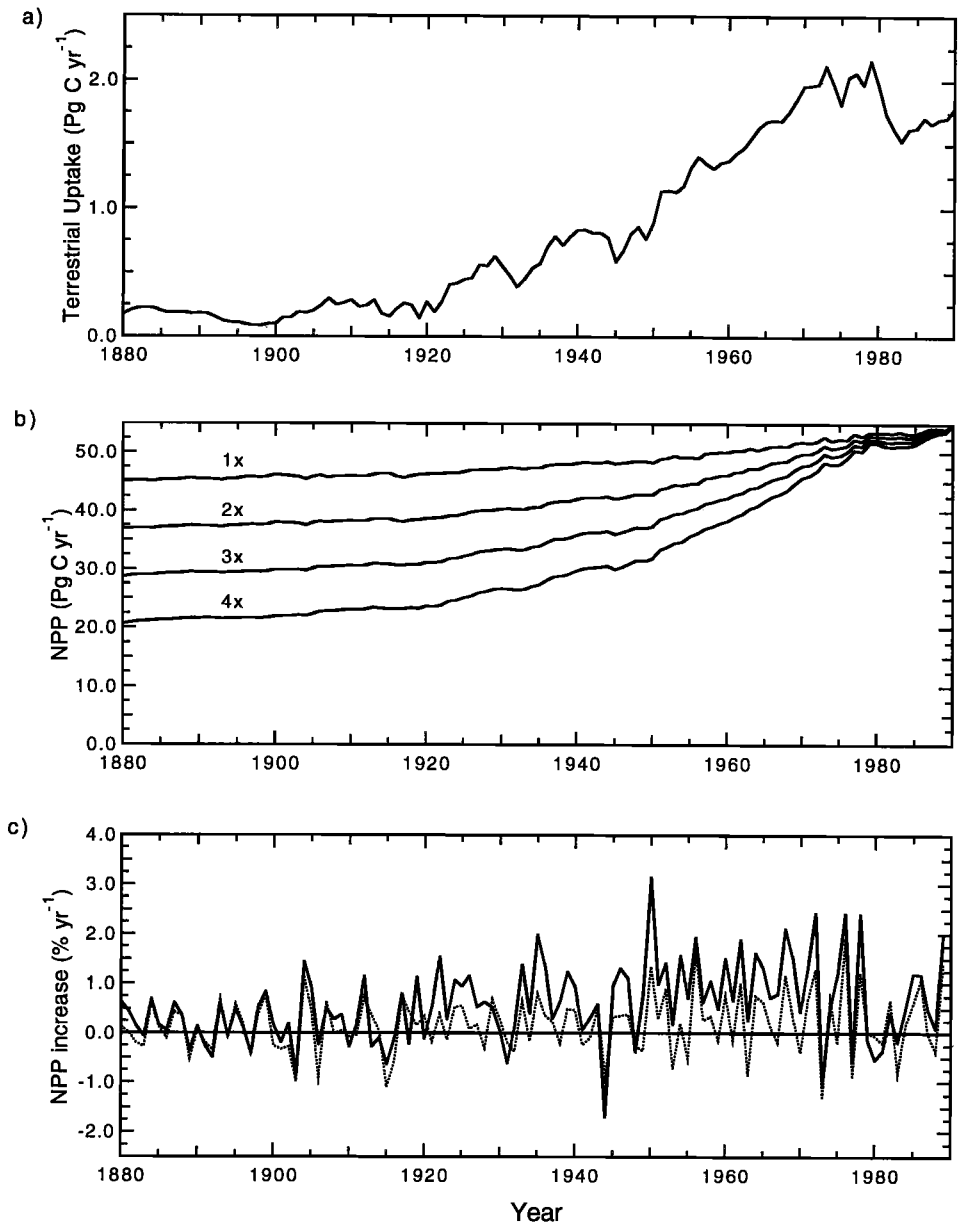

Figure 5. (a) Historical estimate of the terrestrial carbon sink from *Houghton* [1995]. (b) Times series of NPP required with the CASA model to produce NEP multiples of (1x, 2x, 3x, and, 4x) the *Houghton* [1995] estimate shown in Figure 5a. (c) Percent per year change in NPP ([NPP(t) - NPP(t-1)]/NPP(t-1)) for the CASA model runs that matched 1x (dotted line) and 3x (solid line) the *Houghton* [1995] terrestrial carbon sink history shown in Figure 5a.

matched the observed amplitude increases at Arctic stations. In eight tracers, NEP fluxes from the 3 x *Ho* run were partitioned into regions north and south of 60°N, 50°N, 40°N, and 30°N. NEP fluxes for the remaining land area were taken from the constant NPP model run.

The history of the terrestrial carbon sink used here (Figure 5a) is the same as Figure 19.2 of *Houghton* [1995]. It was constructed by adding time series of carbon released from land use [*Houghton*, 1993; *Houghton and Hackler*, 1994] to a deconvolution estimate of net terrestrial uptake obtained by using smoothed atmospheric CO_2 data and an ocean general circulation model [*Sarmiento et al.* 1992]. A more recent deconvolution analysis with the high-resolution Law Dome ice core yields a similar history of terrestrial uptake in recent decades (~1.7 Pg C yr^{-1} from 1960 to 1990) [*Bruno and Joos*, 1997]. Much of the uncertainty in these deconvolution estimates of a terrestrial carbon sink comes from our limited understanding of the processes that control carbon release following anthropogenic disturbance.

Because the *Houghton* [1995] sink estimates are available only as annual sums, we assumed that our year-to-year adjustments in NPP to match the sink estimates occurred monthly in proportion to the steady state seasonal cycle of NPP for each grid cell. If, for example, a 0.2% increase in

annual NPP was required from one year to the next to satisfy the sink, then each monthly NPP value at each grid cell was increased by 0.2%. For the 1° x 1° grid cell resolution of CASA this assumption should be consistent with several proposed causes of the sink. While the relative impacts of CO_2 or N fertilization may be greatest at the beginning or at the end of the growing season, during periods of water and temperature stress, these are times when absolute rates of net photosynthesis are low because APAR is low. In the middle of the growing season, high LAIs, favorable temperatures, and available soil water provide the capacity for high photosynthetic rates and high absolute returns on CO_2 or N fertilization.

In the case of CO_2 and nitrogen fertilization interacting with forest regrowth a probable long-term effect would be an acceleration of the rate of biomass accumulation. While greater aboveground biomass in perennials may provide the capacity for a higher leaf area, and thus greater light interception and CO_2 uptake, it is not evident that a significant shift in the seasonal cycle of NPP would follow. It is important to note, however, that terrestrial uptake associated only with forest regrowth may occur with increases or even decreases in NPP, depending on the age of the forest [e.g., *Gower et al.*, 1996].

3. Results

3.1. Trends in NOAA/CMDL Flask Station Network

All of the Arctic and subarctic stations north of 55°N (Alert, Mould Bay, Point Barrow, Ocean Station M, and Cold Bay) show a similar pattern of month-to-month variation in interannual CO_2 growth rates (Figure 6). The highest growth rates occur during winter and early spring (December, January, February, and March) while the lowest rates occur during summer and early fall (June, July, August, and September). At Alert, Mould Bay, and Point Barrow the amplitude has significantly increased (Table 1). Of these three stations, Alert and Mould Bay exhibit the strongest seasonal variation in growth rates (Figure 6) and the greatest increases in amplitude (Table 1). The increase in amplitude for the five stations north of 55°N combined was 0.66% yr^{-1} for the period 1981 to 1995 ($p \leq 0.01$; see Figure 7).

We also estimated the rate of change of the downward zero crossing time of the CO_2 seasonal cycle for stations north of 55°N [*Keeling et al.*, 1996]. For the five stations north of 55°N combined, the downward zero crossing advanced at a rate of 2.48 days per decade for the period 1981 to 1995.

The amplitude increases and the associated seasonal pattern of interannual CO_2 growth rates for Arctic stations do not persist further south (Table 1, Figure 6). At Shemya, Cape Meares, and Niwot Ridge there is a reversal of the Arctic seasonal pattern of CO_2 growth rates. For this set of stations, CO_2 growth rates are the highest during summer months and early fall. This pattern suggests that in the future, T_{amp} may decrease for these stations, though at present the trends are not significant. South of this cluster the Arctic seasonal pattern of low interannual CO_2 growth rates during summer months reappears at Midway, Kumukahi, and Guam Island, though T_{amp} estimates for these stations also are not significant.

At the Seychelles, Ascension, and Samoa Island stations in the southern hemisphere the amplitude has increased rapidly (Table 1). These three stations are all within a latitude band of 5°S to 15°S and may be influenced by changing spatial and temporal patterns of fossil fuel combustion and biomass burning. It is important to note, however, that (1) the absolute changes in the seasonal cycle of CO_2 are small and (2) it is difficult to extract the seasonal cycle from the interannual trend in the southern hemisphere because the amplitudes are of the same order of magnitude as the interannual CO_2 growth rates (~1.6 ppm yr^{-1} for the period of the 1980s [*Conway et al.*, 1994]).

3.2. Footprints of Terrestrial Ecosystems at Observation Stations

The GISS tracer model driven by surface fluxes from terrestrial steady state NEP, fossil fuels, biomass burning, and ocean exchange does a mixed job of reproducing the NOAA/CMDL seasonal cycle at a number of observation stations (Figure 8). At high-latitude stations in the northern hemisphere the amplitude of the modeled seasonal cycle is approximately 30% less than that observed (Tables 1 and 4). In the northern hemisphere the modeled seasonal cycle is highly correlated with the observations (for all stations $r \geq 0.93$; Table 4). In the southern hemisphere the correlation with observations is lowest for Seychelles, Ascension, and Samoa Islands (r = 0.62, 0.64, and 0.62, respectively).

A sharp transition exists in the contribution of the terrestrial steady state NEP to the seasonal cycle for stations north and south of the equator (Table 4). North of the equator, the contribution of NEP ranges from 71% at Christmas Island (2°00'N) to 92% at Mould Bay (76°14'N). South of the equator the contribution ranges from 34% at Cape Grim, Tasmania (40°41'S) to 59% at Ascension Island (7°55'S). Fluxes from oceans, biomass burning, and fossil fuel emissions contribute substantially more to the seasonal cycle in the southern hemisphere than in the northern hemisphere (Table 4).

Results from the biome tracer experiment (Figure 2a) indicate that boreal forests (tracer 1.2) have the greatest impact on the seasonal cycle of CO_2 concentrations at observation stations in the northern hemisphere (Table 5). At Arctic and subarctic stations north of 55°N the contribution of boreal forests to the terrestrial biosphere component of the seasonal cycle ranges from 34% to 42%. At Mauna Loa and Kumukahi, boreal forests comprise 24-25% of the terrestrial biosphere signal.

For stations north of 55°N the adjacent tundra biome (tracer 1.1) exerts the most influence on the seasonal cycle per unit of GSNF (tundra has a GSNF of 0.42 Pg C yr^{-1} whereas boreal forest has a GSNF of 2.08 Pg C yr^{-1}). In comparison with boreal forests (tracer 1.2) and deciduous forests (tracer 1.3), the contribution of the tundra biome to the seasonal cycle falls off more quickly for stations closer to the equator (Table 5).

While the tropical forests (tracer 1.8) have a GSNF almost identical to that of boreal forests (~2.1 Pg C yr^{-1}), they contribute only minimally to the terrestrial biosphere component of the seasonal cycle at observation stations at middle and high latitudes in the northern hemisphere (from 2.8% at Alert to 4.4% at Key Biscayne). At stations further south the signature of tropical forests increases, reaching 18% at Christmas Island (2°00'N).

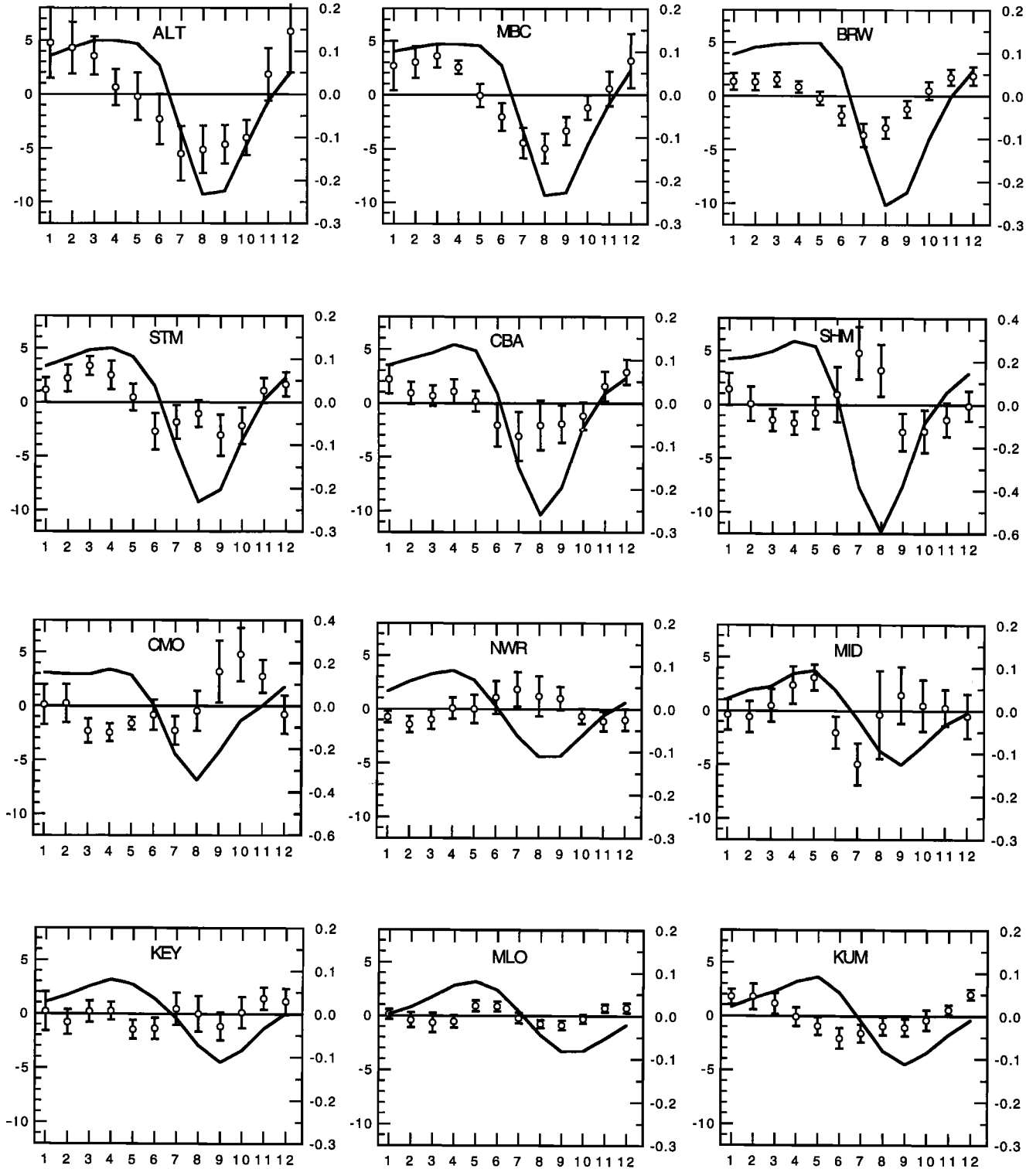

Figure 6. Detrended mean seasonal cycle of CO_2 (in parts per million) for the stations listed in Table 1 (dotted line, left axis). Monthly CO_2 growth rates (in parts per million per year) for the detrended time series and standard deviations calculated as described in section 2.1 (circles with standard deviation error bars, right axis). Note that the scale on the right axis for SHM and CMO extends from -0.6 to 0.4 ppm yr^{-1}, twice the range of the other plots in this series.

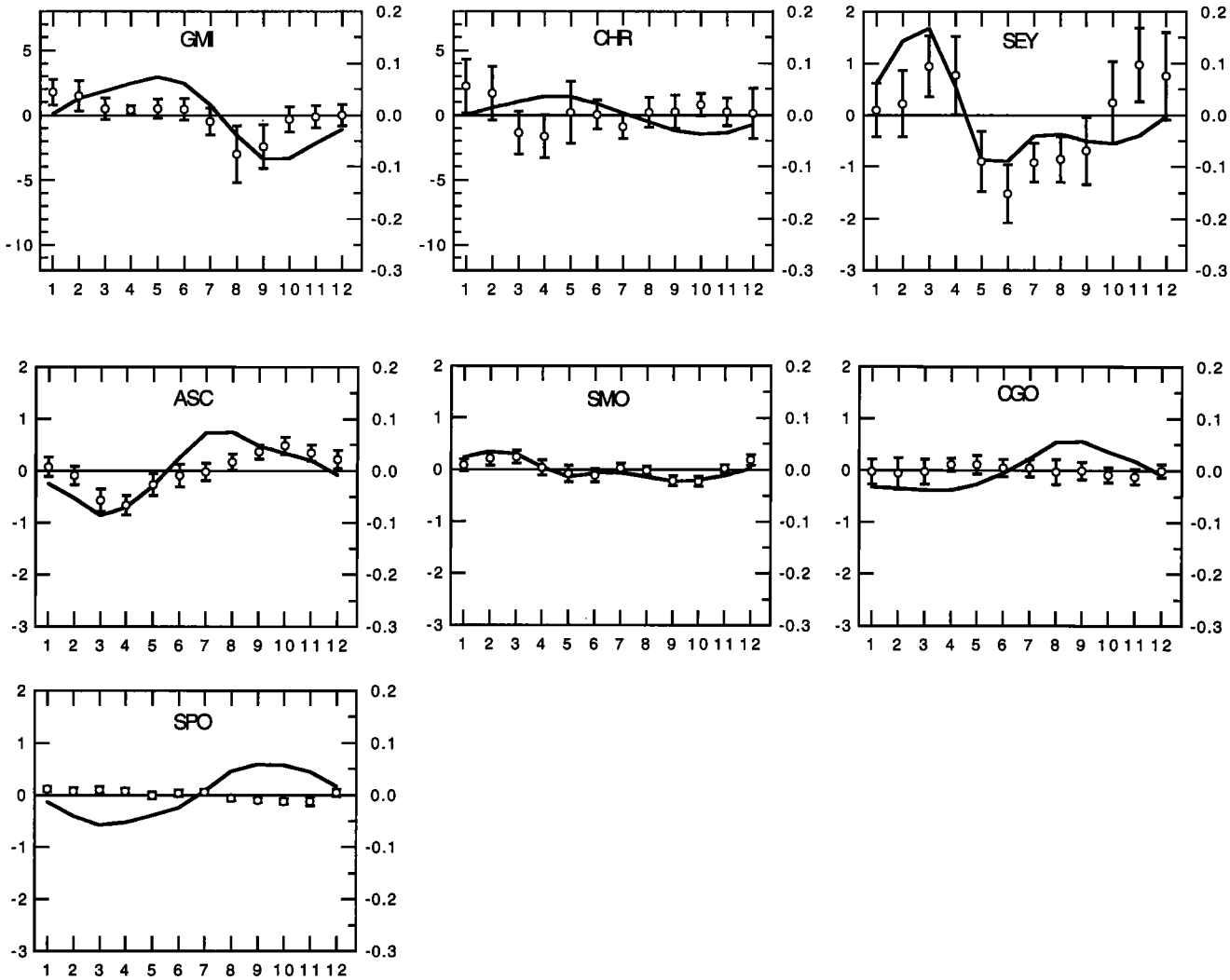

Figure 6. (continued)

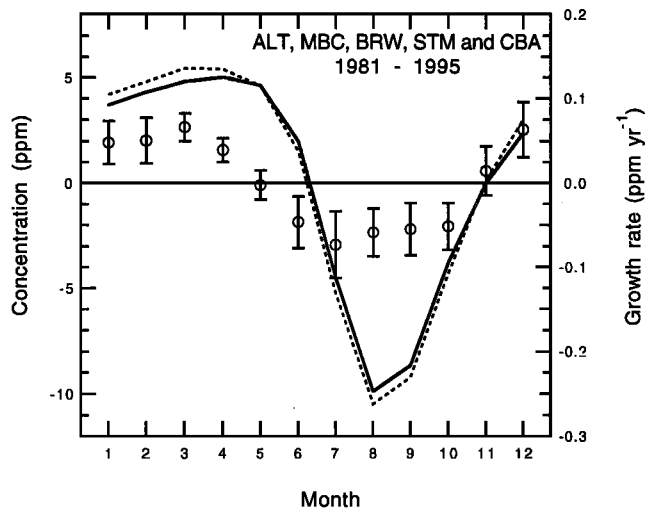

Results from the latitude band tracer experiment (Figure 2b) further demonstrate that high-latitude ecosystems in the northern hemisphere are dominant contributors to the seasonal cycle at observation stations in both the northern and southern hemisphere. Ecosystems north of 50°N contribute between 34% and 65% of the total terrestrial biosphere signal at stations in the northern hemisphere. At Mauna Loa, 70% of the terrestrial biosphere signal is driven by ecosystems north of 40°N (Table 5).

The minimum contribution of agricultural regions to terrestrial biosphere component of the seasonal cycle occurs at Point Barrow (14.1%). The maximum occurs at Seychelles

Figure 7. Detrended seasonal cycle (solid line) and monthly growth rate (circles with standard deviation error bars) for the combination of all stations north of 55°N (Alert, Mould Bay, Point Barrow, Station M, and Cold Bay) from 1981 to 1995. The dotted line is the projected seasonal cycle in 10 years, assuming the detrended seasonal pattern of interannual CO_2 growth rates remains unchanged [*Manning*, 1993].

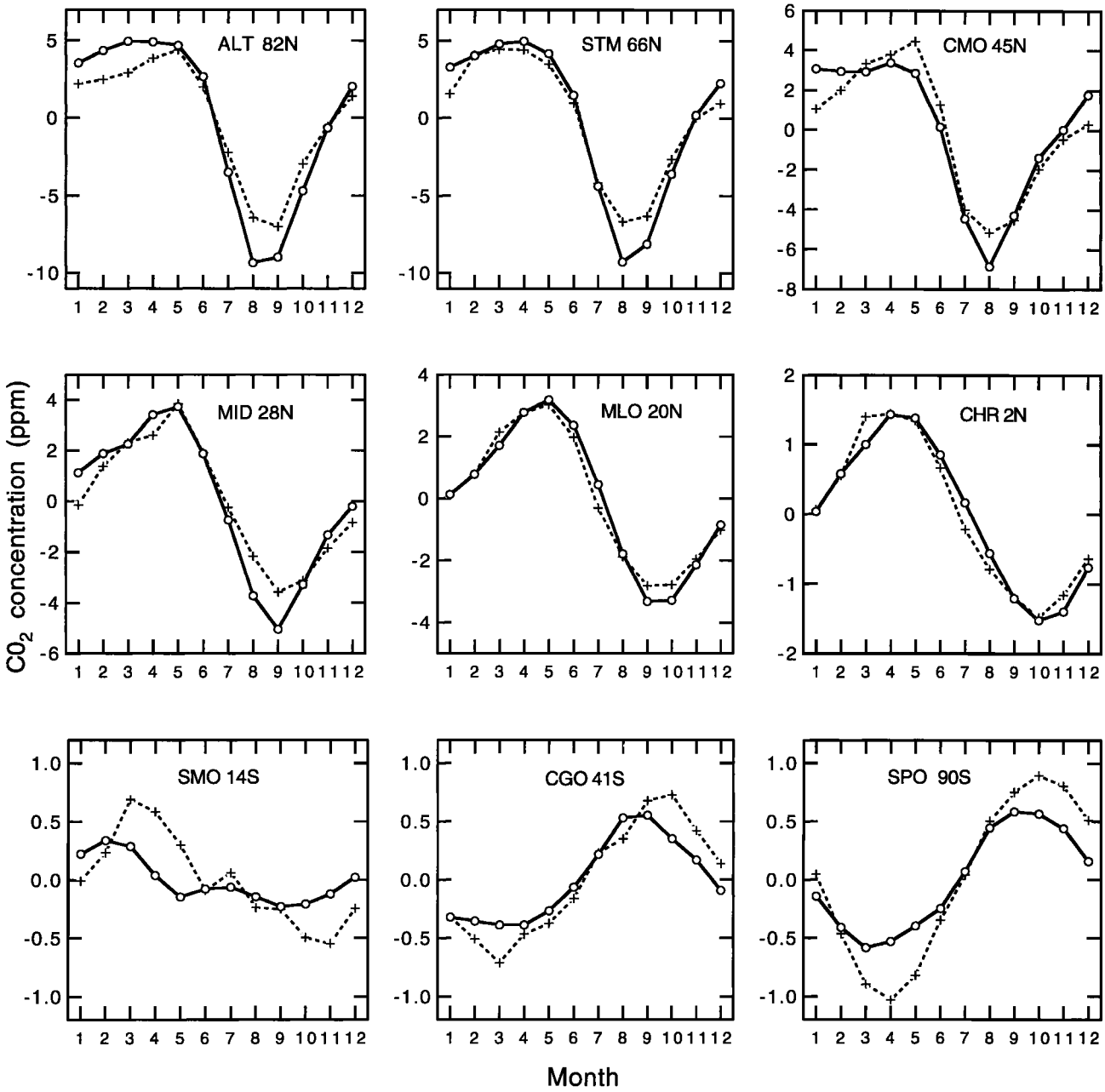

Figure 8. Modeled estimates (dotted lines, crosses) of the detrended seasonal cycle for nine of the 19 stations listed in Table 1. The model estimates were obtained by driving the GISS tracer model with surface fluxes from steady state terrestrial NEP, fossil fuel emissions, biomass burning, and ocean exchange. The detrended seasonal cycle for the NOAA/CMDL observation stations (Table 1) is shown for comparison (solid line, circles).

(34.7%). Approximately 20% of the terrestrial biosphere signal at midlatitude stations in the northern hemisphere has an agricultural origin (Table 5).

Ecosystems and regions that contribute the most to the seasonal cycle of CO_2 concentrations at stations in the northern hemisphere, such as tundra, boreal forests, mixed deciduous forests, and agriculture regions north of 40°N, are also in phase with the observed seasonal cycle from the NOAA/CMDL time series (Table 6). Thus an increase in the seasonality of NEP fluxes from one or more of these regions will increase the amplitude of the seasonal cycle at many of the observation stations in the northern hemisphere. The terrestrial biosphere in the southern hemisphere contributes only modestly to the seasonal cycle at northern hemisphere stations.

In contrast, northern hemisphere terrestrial ecosystems contribute substantially to the seasonal cycle at many stations in the southern hemisphere. Because of lags in transport and nonoverlapping growing seasons, some components from the northern and southern hemisphere are out of phase with one

Table 4. Terrestrial Biosphere, Fossil Fuel, Biomass Burning, and Ocean Tracers

			Percent Contribution to the Seasonal Cycle[b]: Equation (2)				Correlation With NOAA/CMDL Seasonal Cycle: Equation (3)				
Station	Lattitude °N	Modeled Amplitude[a]	Terrestrial Biosphere	Fossil Fuels	Biomass Burning	Oceans	All Fluxes	Terrestrial Biosphere	Fossil Fuels	Biomass Burning	Oceans
ALT	82	11.4	90.3	5.9	1.4	2.3	0.99	0.99	0.89	-0.55	0.56
MBC	76	13.3	92.1	4.0	1.6	2.3	0.96	0.96	0.92	-0.42	0.59
BRW	71	13.3	91.2	4.3	1.6	2.9	0.93	0.93	0.69	-0.32	0.77
STM	66	11.1	83.6	9.2	1.3	5.9	0.99	0.99	0.58	-0.24	0.57
CBA	55	10.3	86.5	6.6	2.0	4.9	0.93	0.94	0.89	-0.53	0.71
SHM	53	10.7	81.5	7.8	2.5	8.1	0.93	0.94	0.92	-0.56	0.69
CMO	45	9.6	89.6	5.2	1.5	3.7	0.97	0.98	0.78	-0.28	-0.94
NWR	40	9.0	89.7	5.9	2.3	2.1	0.95	0.95	0.83	-0.49	-0.92
MID	28	7.4	73.4	15.3	2.3	8.9	0.96	0.97	0.87	-0.27	-0.88
KEY	25	6.9	79.4	14.3	4.3	2.1	0.95	0.97	0.46	0.27	-0.83
MLO	20	5.8	81.6	14.3	2.3	1.8	0.99	0.99	0.92	0.06	-0.36
KUM	20	6.1	82.0	13.7	2.2	2.2	0.98	0.98	0.94	-0.15	-0.11
GMI	13	3.4	79.8	15.2	3.6	1.3	0.99	0.98	0.23	0.84	0.00
CHR	2	2.9	71.6	12.4	3.8	12.2	0.98	0.99	0.81	-0.36	0.02
SEY	-5	0.9	49.0	25.3	8.3	17.4	0.62	-0.13	0.70	0.12	0.65
ASC	-8	2.2	59.1	13.3	13.7	13.9	0.64	0.83	-0.94	0.23	-0.97
SMO	-14	1.2	46.7	13.5	10.4	29.4	0.62	-0.03	0.67	0.14	0.89
CGO	-41	1.4	33.8	8.5	18.2	39.4	0.93	0.94	0.36	-0.28	0.94
SPO	-90	1.9	43.1	5.7	12.5	38.8	0.97	0.99	0.49	-0.32	0.95

[a]The amplitude of the seasonal cycle was obtained by using the GISS model with surface fluxes from the terrestrial biosphere, fossil fuels, biomass burning, and oceans.
[b]At each station the contribution from each of the four tracers sums to 100%.

another. Thus an increase in seasonal cycle of NEP fluxes from terrestrial ecosystems in the northern hemisphere could drive a decrease in the amplitude of the seasonal cycle of atmospheric CO_2 at stations in the southern hemisphere.

3.3. Impacts of Anthropogenic Forcing on Trends in the Seasonal Cycle

3.3.1. Biomass burning. At stations in the northern hemisphere the contribution of biomass burning to the seasonal cycle ranges from 1% to 4% (Table 4). For midlatitude and high-latitude stations in the northern hemisphere the biomass burning tracer is weakly and negatively correlated with the mean seasonal cycle from the NOAA/CMDL observations (Table 4). The effect of biomass burning on amplitude trends appears minimal for most stations in the northern hemisphere outside the tropics (Table 7). Amplitude trends estimated by using a seasonal cycle derived from both modeled fluxes and NOAA/CMDL

Table 5. Percent Contribution From Tracers to the Terrestrial Biosphere Component of the Seasonal Cycle at Observation Stations (Equation (2))

		Ecosystems										Latitude Bands					Agriculture	
		1.1,	1.2,	1.3,	1.4,	1.5,	1.6,	1.7,	1.8,	1.9,	1.10,	2.1,	2.2,	2.3,	2.4,	2.5,	3.1,	3.2,
Station	Latitude °N	Tundra	Boreal Forests	Deciduous Forests	AGS[a] >40°N	AGS[a] 20°N to 40°N	AGS[a] 0°N to 20°N	Shrublands, Deserts	Tropical Forests	AGS[a] 0°S to 60°S	Forests 0°S to 60°S	North of 60°N	50°N to 60°N	40°N to 50°N	30°N to 40°N	South of 30°N	Agriculture	No Agriculture
ALT	82	10.3	36.3	15.0	21.0	5.4	4.8	0.6	2.8	3.8	0.1	23.7	32.6	28.0	8.3	7.3	18.1	81.9
MBC	76	14.0	38.0	13.0	18.8	5.1	4.3	0.5	2.6	3.5	0.1	31.7	30.8	24.0	7.3	6.3	16.1	83.9
BRW	71	14.4	42.0	11.7	15.8	5.2	4.4	0.5	2.6	3.4	0.1	38.1	27.0	21.3	7.3	6.3	14.1	85.9
STM	66	10.4	36.5	15.5	21.1	4.6	4.8	0.5	2.8	3.7	0.1	27.7	31.8	25.9	7.4	7.2	17.3	82.7
CBA	55	9.3	34.4	14.3	19.3	7.8	5.9	0.7	3.5	4.7	0.2	21.4	31.5	27.2	10.7	9.2	17.2	82.8
SHM	53	9.6	33.9	15.1	18.9	7.3	6.0	0.7	3.5	4.9	0.2	19.1	34.3	27.4	10.2	9.0	17.3	82.7
CMO	45	6.6	33.6	12.5	26.5	6.8	5.5	0.8	3.2	4.3	0.1	18.6	35.6	27.8	9.2	8.8	15.8	84.2
NWR	40	4.9	27.9	12.5	33.6	6.9	5.5	1.0	3.1	4.5	0.1	14.2	31.5	35.3	9.8	9.2	23.3	76.7
MID	28	5.6	28.3	14.3	20.0	10.5	8.7	0.9	4.4	7.2	0.2	16.7	28.5	28.5	13.3	13.1	19.7	80.3
KEY	25	4.7	24.4	17.9	22.6	10.4	8.3	0.8	4.4	6.3	0.2	12.6	24.7	30.0	22.3	10.3	28.2	71.8
MLO	20	4.5	23.9	13.2	19.9	10.4	10.2	0.9	7.4	9.4	0.3	14.4	27.2	28.1	13.2	17.2	20.3	79.7
KUM	20	4.6	24.9	13.4	20.3	10.3	9.7	0.9	6.9	8.8	0.3	14.5	27.8	28.3	13.0	16.4	20.0	80.0
GMI	13	3.3	16.4	10.6	14.7	11.3	14.8	0.8	10.9	16.5	0.5	12.5	22.7	25.9	16.2	22.7	22.6	77.4
CHR	2	2.6	13.6	8.3	12.0	6.9	15.7	0.5	18.1	21.3	1.0	12.1	21.9	25.2	12.3	28.6	22.1	77.9
SEY	-5	2.5	12.2	7.7	10.4	9.4	17.0	0.6	6.7	32.7	1.0	13.3	23.7	26.5	14.3	22.3	34.7	65.3
ASC	-8	1.3	6.9	4.2	5.6	4.6	13.2	0.3	5.6	56.1	2.2	4.9	8.6	9.5	4.6	72.4	18.5	81.5
SMO	-14	2.0	10.4	6.6	9.4	5.6	15.3	0.4	16.6	33.1	0.5	12.3	22.3	25.9	12.6	26.9	33.6	66.4
CGO	-41	1.8	9.2	5.7	7.9	5.5	14.2	0.3	7.2	39.6	8.5	10.1	18.5	20.3	10.4	40.7	16.0	84.0
SPO	-90	1.9	10.1	6.3	8.8	5.9	15.5	0.3	7.7	37.9	5.4	8.0	14.5	16.4	8.1	52.9	20.1	79.9

Tracer flux characteristics are given in Table 3. Each set of tracers (ecosystems, latitude bands, and agriculture) sums to 100% at each station.
[a]Agriculture, grasslands, and savannas (or open woodlands in C3 regions).

Table 6. Correlation Between Tracers and the Observed Seasonal Cycle at NOAA/CMDL Observation Stations (Equation (3))

		Ecosystems										Latitude Bands					Agriculture	
		1.1,	1.2,	1.3,	1.4,	1.5,	1.6,	1.7,	1.8,	1.9,	1.10,	2.1,	2.2,	2.3,	2.4,	2.5,	3.1,	3.2,
Station	Latitude °N	Tundra	Boreal Forests	Deciduous Forests	AGS[a] >40°N	AGS[a] 20°N to 40°N	AGS[a] 0°N to 20°N	Shrublands, Deserts	Tropical Forests	AGS[a] 0°S to 60°S	Forests 0°S to 60°S	North of 60°N	50°N to 60°N	40°N to 50°N	30°N to 40°N	South of 30°N	Agriculture	No Agriculture
ALT	82	0.96	0.98	1.00	0.99	0.64	-0.72	0.82	-0.70	0.94	0.92	0.96	0.99	0.99	0.89	-0.42	0.99	0.98
MBC	76	0.80	0.90	0.98	0.99	0.65	-0.72	0.78	-0.68	0.92	0.90	0.77	0.96	0.98	0.88	-0.41	0.98	0.94
BRW	71	0.75	0.85	0.98	0.98	0.70	-0.66	0.74	-0.62	0.90	0.89	0.70	0.95	0.97	0.90	-0.31	0.96	0.90
STM	66	0.95	0.99	0.97	0.96	0.51	-0.69	0.79	-0.69	0.91	0.88	0.95	0.99	0.98	0.85	-0.45	0.97	0.99
CBA	55	0.96	0.96	0.94	0.93	0.67	-0.66	0.75	-0.61	0.91	0.90	0.95	0.98	0.92	0.88	-0.28	0.88	0.94
SHM	53	0.94	0.94	0.94	0.91	0.63	-0.68	0.76	-0.63	0.89	0.88	0.94	0.96	0.90	0.85	-0.35	0.87	0.94
CMO	45	0.93	0.94	0.98	0.92	0.76	-0.54	0.58	-0.49	0.90	0.86	0.93	0.94	0.98	0.95	-0.11	0.97	0.97
NWR	40	0.85	0.97	0.94	0.83	0.75	-0.58	0.34	-0.43	0.90	0.85	0.92	0.97	0.87	0.87	-0.07	0.90	0.96
MID	28	0.91	0.96	0.98	0.98	0.93	0.02	0.42	0.41	0.41	0.19	0.93	0.98	0.98	0.98	0.58	0.96	0.96
KEY	25	0.94	0.99	0.77	0.93	0.81	0.40	0.49	0.54	0.07	-0.28	0.96	0.99	0.93	0.52	0.69	0.84	0.99
MLO	20	0.96	0.99	0.99	0.95	0.99	0.59	0.17	0.94	-0.32	-0.75	0.98	0.98	0.98	0.93	0.93	0.99	0.99
KUM	20	0.89	0.96	0.98	0.98	0.94	0.36	0.34	0.83	-0.04	-0.55	0.93	0.98	0.98	0.97	0.83	0.98	0.98
GMI	13	0.77	0.93	1.00	1.00	0.99	0.58	0.35	0.85	-0.44	-0.46	0.86	0.98	0.99	0.94	0.85	0.99	0.98
CHR	2	0.65	0.83	0.98	0.99	0.91	0.90	0.41	0.87	-0.87	-0.96	0.74	0.91	0.97	0.99	0.72	0.98	0.98
SEY	-5	-0.33	-0.21	0.00	0.05	-0.02	-0.26	0.91	-0.44	0.15	0.74	-0.26	-0.10	-0.02	0.28	-0.28	-0.06	-0.17
ASC	-8	0.54	0.35	-0.04	-0.11	0.16	-0.47	-0.48	0.21	0.79	0.90	0.43	0.16	-0.01	-0.35	0.84	0.73	0.84
SMO	-14	-0.56	-0.38	-0.05	-0.02	-0.30	-0.23	0.80	0.43	0.08	-0.18	-0.48	-0.24	-0.09	0.21	0.30	-0.14	0.02
CGO	-41	0.96	0.99	0.87	0.85	0.96	0.78	-0.38	0.14	-0.18	-0.51	0.99	0.96	0.90	0.66	0.18	0.38	0.87
SPO	-90	0.98	0.99	0.87	0.84	0.96	0.79	-0.38	0.16	0.31	0.31	1.00	0.96	0.89	0.66	0.88	0.88	0.97

Tracer flux characteristics are given in Table 3.
[a]Agriculture, grasslands, and savannas (or open woodlands in C3 regions).

Table 7. Amplitude Trends Induced by Fossil Fuel Emissions and Biomass Burning

		Trends Induced by Fossil Fuel Emissions, % yr^{-1}						Trends Induced by Biomass burning, % yr^{-1}	
		1961 to 1990		1971 to 1990		1981 to 1990		1971 to 1990	
Station	Latitude °N	GISS Baseline[a]	NOAA/ CMDL[b]	GISS Baseline[a]	NOAA/ CMDL[b]	GISS Baseline[a]	NOAA/ CMDL[b]	GISS Baseline[a]	NOAA/ CMDL[b]
ALT	82	0.07	0.13	0.04	0.11	0.02	0.09	-0.01	-0.02
MBC	76	0.06	0.07	0.03	0.05	0.01	0.02	-0.02	-0.02
BRW	71	0.13	0.11	0.10	0.08	0.09	0.08	-0.01	-0.01
STM	66	0.13	0.10	0.09	0.02	0.06	-0.07	-0.02	-0.01
CBA	55	0.16	0.10	0.09	0.06	0.08	0.05	-0.04	-0.02
SHM	53	0.17	0.09	0.09	0.05	0.07	0.04	-0.04	-0.02
CMO	45	0.23	0.15	0.19	0.10	0.19	0.11	-0.01	-0.02
NWR	40	0.08	0.07	0.04	0.03	0.03	0.03	-0.04	-0.03
MID	28	0.27	0.20	0.14	0.11	0.15	0.11	-0.02	-0.02
KEY	25	0.19	0.09	0.12	0.05	0.16	0.07	-0.02	0.03
MLO	20	0.24	0.20	0.16	0.13	0.20	0.17	0.02	0.02
KUM	20	0.24	0.17	0.16	0.11	0.20	0.14	0.01	0.01
GMI	13	-0.08	0.02	-0.12	-0.01	-0.19	-0.01	0.14	0.07
CHR	2	0.23	0.21	0.16	0.14	0.31	0.21	-0.08	-0.01
SEY	-5	0.04	0.29	-0.01	0.23	-0.18	0.33	-0.39	0.03
ASC	-8	-0.44	-1.11	-0.42	-1.02	-0.65	-1.48	-0.07	0.79
SMO	-14	0.61	0.95	0.45	0.79	0.58	0.95	-0.39	0.17
CGO	-41	0.08	0.10	0.04	0.01	0.04	0.28	0.01	0.00
SPO	-90	-0.06	0.24	-0.10	0.20	-0.10	0.22	-0.05	-0.23

[a]Amplitude trends were calculated by using a steady state seasonal cycle of atmospheric CO_2 that was obtained from the GISS tracer model driven by ocean fluxes and steady state NEP fluxes from the CASA model run. For the fossil fuel induced trend estimates, 1990 biomass burning fluxes were also used to calculate the seasonal cycle. Likewise, for the biomass burning induced trends, 1990 fossil fuel emissions were used to calculate the seasonal cycle of atmospheric CO_2.

[b]Amplitude trends were also calculated by adding the observed, detrended seasonal cycle from the NOAA/CMDL observation stations to the modeled CO_2 concentrations from fossil fuel emissions and biomass burning. Using the NOAA/CMDL observation to construct a seasonal cycle may underestimate the trend, since biomass burning and fossil fuels components are already represented in the observations. The advantage to using the NOAA/CMDL observations over the modeled seasonal cycle is that in the modeled derived seasonal cycle, errors introduced from one tracer, in either phase or magnitude, could alter the predicted trend.

observations (section 2.3.3) were less than ±0.05% yr^{-1} for stations north of Guam Island.

In the southern hemisphere the contribution of biomass burning to the seasonal cycle is significantly greater than that in the north. Consequently, in the southern hemisphere, with the imposed changes in burning from 1971 to 1990, the amplitude trends are greater and vary more widely (Table 7).

3.3.2. Fossil fuel emissions. In the northern hemisphere the contribution of fossil fuels to the seasonal cycle gradually increases from 5% at Alert to over 17% at Midway Island (Figure 9). While the contribution of fossil fuel emissions is small in comparison with the terrestrial biosphere component for stations in the northern hemisphere, fossil fuel emissions cannot be neglected in evaluations of tracer model performance.

At many stations in the southern hemisphere, fossil fuel emissions appear to be critical component of the seasonal cycle. Seychelles, Ascension, and Samoa Islands show extreme sensitivity to fossil fuel emissions. At Seychelles the contribution of fossil fuels increased from 22% in 1961 to 42% in 1990 (Figure 9).

At Arctic and subarctic stations north of 55°N, increasing rates of fossil fuel emission generated T_{amp} values between 0.07% yr^{-1} and 0.16% yr^{-1} for the period 1961 to 1990 (Table 7). When more recent sampling periods are considered, T_{amp} estimates from fossil fuel emissions decrease for these northern stations. This decrease reflects a stabilization of fossil fuel consumption in northern industrial countries during the 1980s. Between 1980 and 1990, fossil fuel emissions remained constant or even declined for regions north of 45°N [*Andres et al.*, 1996] (Figure 3b).

At Mauna Loa the observed increase in the amplitude of the seasonal cycle appears to have a sizable component due to changing fossil fuel emissions. Estimates of T_{amp} for this station from fossil fuel emissions range from 0.13% yr^{-1} for the 1971 to 1990 period to 0.24% yr^{-1} for the 1961 to 1990 period (Table 7).

3.3.3. NPP stimulation. A fairly uniform meridional distribution of amplitude increases is observed for each of the five CASA-GISS model runs that were executed to determine the changes in NPP required to span the high-latitude amplitude increases (Figure 10). This meridional distribution is what might be expected under a uniform, relative NPP forcing of all ice-free land area over a period of several decades. Over shorter sampling periods, more station-to-station variability appears that may be driven by variability in temperature and soil moisture acting on heterotrophic respiration (data not shown).

In the CASA-GISS model run in which NPP was constant, the only source of interannual variation in NEP fluxes was from monthly temperature and precipitation anomalies acting on heterotrophic respiration. No significant increase in the amplitude is observed for this run in the northern hemisphere (Figure 10, Table 8). This finding suggests that at the global scale, increasing winter temperatures are insufficient to substantially change the amplitude of the seasonal cycle independent of changes in NPP.

At stations north of 55°N the 3 x *Ho* run generates amplitude trends similar to observations (a modeled trend of 0.62% yr^{-1} for 1981 to 1990 versus the observed trend of 0.66% yr^{-1} for 1981 to 1995; see Table 8). Global terrestrial uptake for this run, however, is 5.0 Pg C yr^{-1} from 1981 to 1990 (Table 8), a figure incompatible with our current understanding of the carbon cycle [e.g., *Melillo et al.*, 1996]. Spatially partitioning and combining the NEP time series from the 3 x *Ho* run with the NEP time series from the constant NPP run allowed us to answer the second question posed in section 2.3.3: whether it would be possible to reproduce the high-latitude amplitude increases and also obtain reasonable global sink estimates. As described in section 2.3.3., eight

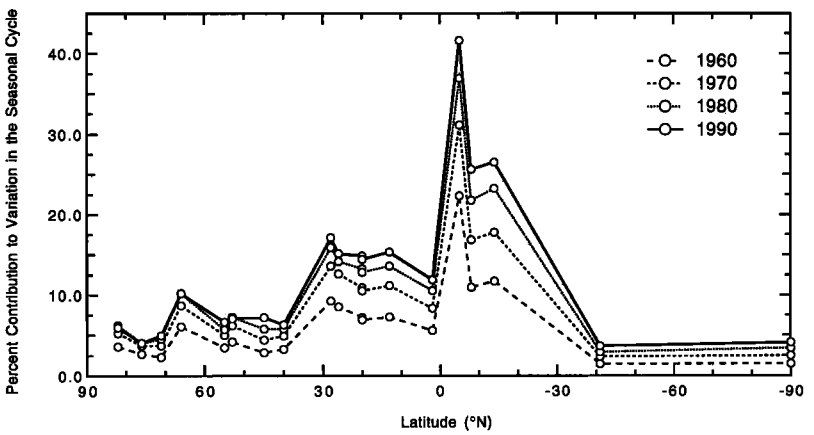

Figure 9. Percent contribution of fossil fuels to the seasonal cycle for 1960, 1970, 1980, and 1990. Note the rapid increase in the fossil fuel contribution in recent decades at low latitude stations in the southern hemisphere. The contribution of fossil fuels was calculated by using two tracers in equation (2). One of the tracers consisted of fossil fuel emissions from 1960, 1970, 1980, or 1990 as described in section 2.3.2. The other tracer consisted of the sum of ocean exchange, biomass burning, and steady state terrestrial NEP. When NOAA/CMDL observations were used to construct the denominator in equation (2) instead of the modeled concentrations from the tracers described above, even larger fossil fuel contributions were estimated for low-latitude stations in the southern hemisphere (data not shown).

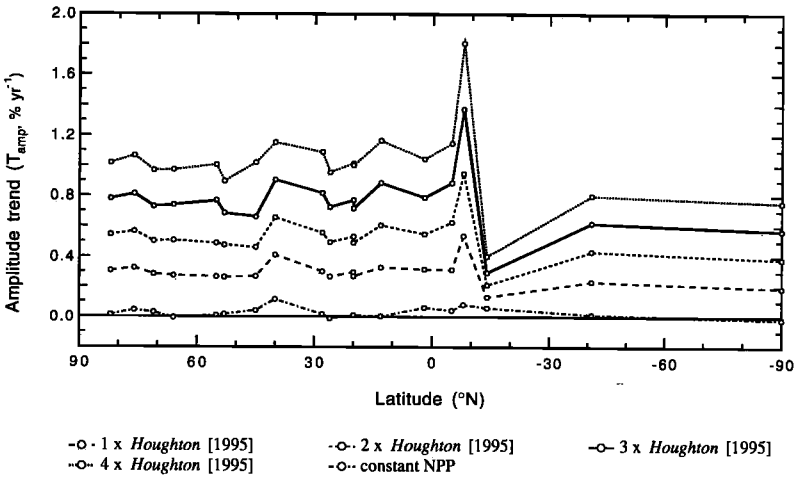

Figure 10. Amplitude trends resulting from NPP increases required to produce carbon sinks equivalent to multiples of the historical sink estimate of *Houghton* [1995]. Values of T_{amp} induced from NPP increases are shown for the period 1961 to 1990. The 5 CASA-GISS model runs shown in this figure comprise experiment 1 in the NPP stimulation analysis.

GISS model runs were performed, using 3 x *Ho* NEP time series from one of eight geographic regions: north of 60°N, 50°N, 40°N, and 30°N and south of 60°N, 50°N, 40°N, and 30°N. These time series were supplemented by NEP time series from the constant NPP run in the remaining land surface area.

Distinct meridional gradients in T_{amp} are generated depending on where the 3 x *Ho* run was partitioned (Figure 11). For the 1961 to 1990 period the effect of northern partitions on amplitude trends at various stations decreases from the north pole to the south pole (Figure 11). Conversely, the

Table 8. NPP Increases, Terrestrial Uptake, and T_{amp} Estimates for the Model Runs in the NPP Stimulation Experiments

Model Run	NPP Increase, % yr^{-1}			Terrestrial Uptake, Pg C yr^{-1}			Amplitude Trend,[a] % yr^{-1}		
	1961 to 1990	1971 to 1990	1981 to 1990	1961 to 1990	1971 to 1990	1981 to 1990	1961 to 1990	1971 to 1990	1981 to 1990
Experiment 1[b]									
Constant NPP	0.00	0.00	0.00	-0.06	-0.07	-0.08	0.02	0.01	0.03
1 x *Ho*	0.28	0.25	0.26	1.78	1.84	1.63	0.30	0.25	0.30
2 x *Ho*	0.53	0.40	0.42	3.56	3.67	3.31	0.54	0.38	0.46
3 x *Ho*	0.80	0.57	0.60	5.34	5.51	5.00	0.78	0.50	0.62
4 x *Ho*	1.09	0.74	0.78	7.12	7.34	6.68	1.03	0.63	0.78
Experiment 2[c]									
North of 60°N (3 x *Ho*)	0.80	0.57	0.60	0.34	0.35	0.32	0.28	0.18	0.23
North of 50°N (3 x *Ho*)	0.80	0.57	0.60	0.98	1.01	0.92	0.54	0.36	0.43
North of 40°N (3 x *Ho*)	0.80	0.57	0.60	1.50	1.55	1.39	0.73	0.47	0.56
North of 30°N (3 x *Ho*)	0.80	0.57	0.60	1.83	1.88	1.67	0.78	0.50	0.60
South of 60°N (3 x *Ho*)	0.80	0.57	0.60	5.00	5.16	4.68	0.51	0.33	0.42
South of 50°N (3 x *Ho*)	0.80	0.57	0.60	4.36	4.49	4.07	0.25	0.16	0.22
South of 40°N (3 x *Ho*)	0.80	0.57	0.60	3.84	3.95	3.61	0.07	0.04	0.09
South of 30°N (3 x *Ho*)	0.80	0.57	0.60	3.51	3.62	3.33	0.03	0.01	0.05

NPP increases and amplitude trends are linear over the sampling period.

[a]Modeled amplitude trends are calculated for the combination of the five stations north of 55°N in Table 1.

[b]Model runs with NPP increases required to match 1, 2, 3, and 4 times the *Houghton* [1995] history of terrestrial uptake are abbreviated as 1, 2, 3, and 4 x *Ho*. These CASA-GISS model runs were executed to determine the NPP increases required to bracket the high latitude amplitude observations.

[c]NEP fluxes from the 3 x *Ho* run were partitioned in the eight regions listed above in separate GISS tracer model runs. In each GISS model run, NEP fluxes in the remaining land area were taken from the constant NPP model run. These GISS model runs were executed to identify regions that could satisfy constraints from both the high-latitude amplitude increases and realistic global sums of terrestrial uptake.

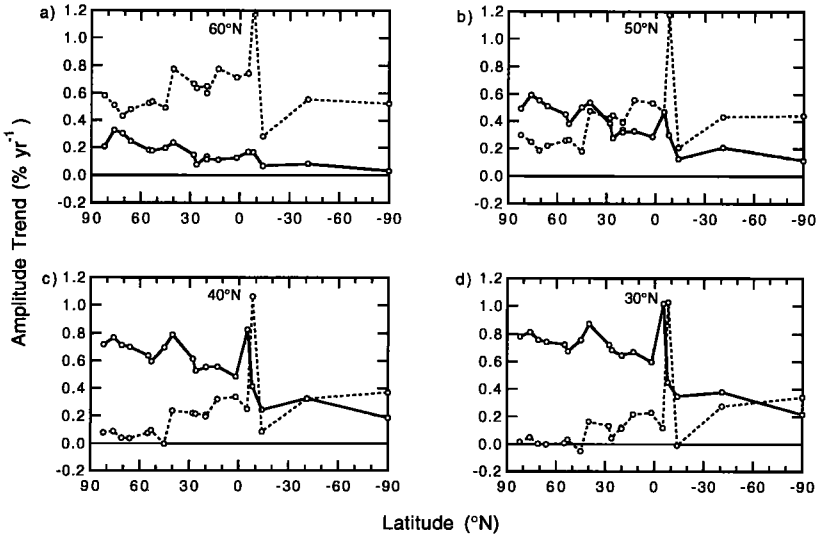

Figure 11. Amplitude trends (T_{amp}) from the 3 x *Ho* model run partitioned into regions north (solid lines) and south (dotted lines) of (a) 60°N, (b) 50°N, (c) 40°N, and (d) 30°N. The eight GISS model runs shown here comprise experiment 2 of the NPP stimulation analysis. The sampling period is 1961 to 1990.

effect of southern partitions on amplitude trends at various stations increases from the north pole to the equator (Figure 11). These meridional patterns are less distinct for the period between 1981 and 1990 because of the greater influence of climate variability on the shorter sampling period (data not shown).

The 3 x *Ho* partition north of 60°N has an average sink of 0.32 Pg C yr^{-1} from 1981 to 1990 and generates amplitude trends of 0.23% yr^{-1} for stations north of 55°N (Table 8). The south of 60°N partition generates larger amplitude trends (0.42% yr^{-1}) for stations north of 55°N, but with a total terrestrial sink of 4.7 Pg C yr^{-1}. Only the GISS runs using partitions north of 30°N or north of 40°N generate amplitude trends comparable to high-latitude observations and terrestrial sinks (<2 Pg C yr^{-1}) comparable to independent estimates (Figure 12). When NPP increases are confined to regions south of 30°N (the south of 30°N partition), a large sink is created with almost no discernible increase in the amplitude for stations north of 55°N (Figure 12).

A comparison of modeled and observed seasonal variation in interannual CO_2 growth rates for stations north of 55°N shows that the coupled CASA-GISS model estimates lag behind observations by approximately 2 months (Figure 13). The model estimates shown in Figure 13 are produced by the 3 x *Ho* partition north of 40°N and the fossil fuel time series described in section 2.3.2. Modeled interannual CO_2 growth

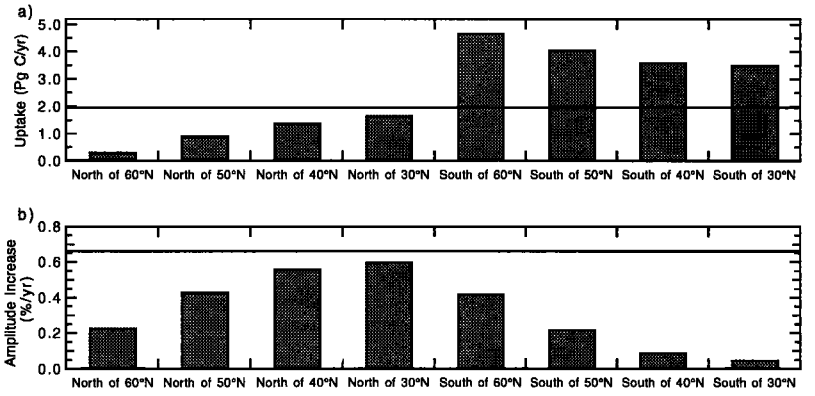

Figure 12. (a) Sum of global terrestrial uptake averaged over the period 1981 to 1990 for the eight GISS tracer model runs that comprised experiment 2 of the NPP stimulation analysis. In each model run, NEP fluxes from the 3 x *Ho* run were confined to the regions denoted on the x axis. (b) Corresponding model estimates of increases in the amplitude of the seasonal cycle of CO_2 for the set of five stations north of 55°N listed in Table 1. Current estimates of terrestrial uptake [*Melillo et al.*, 1996] and amplitude trends for stations north of 55°N (section 3.3) are given by the solid horizontal lines. Realistic model predictions of both terrestrial uptake and the high-latitude amplitude increases are obtained when increases in NPP are confined to broad regions north of 30°N or 40°N.

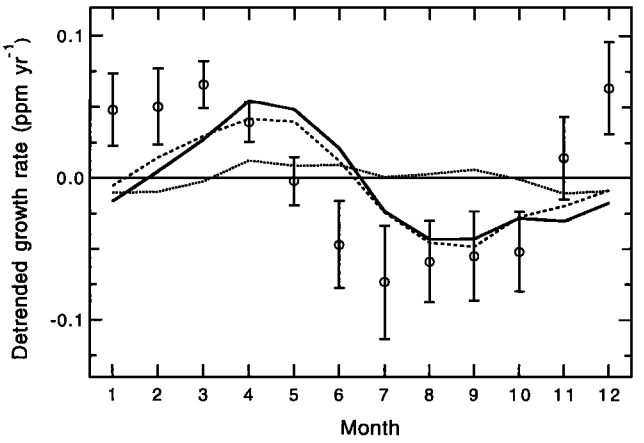

Figure 13. Observed and modeled monthly CO_2 growth rates for the combination of stations north of 55°N in units of parts per million per year. The dashed line is the seasonal pattern of interannual CO_2 growth rates produced by the north of 40°N partition of the 3 x *Ho* model run. The dotted line is the seasonal pattern of interannual CO_2 growth rates produced by fossil fuel emissions. The sum of the two model estimates is given by the solid line. Observations are shown with circles and standard deviation error bars. While the phase of modeled CO_2 concentrations for high-latitude stations almost perfectly matches the observations (Figure 8, Table 4), interannual CO_2 growth rates lag the observations by 2 months. The modeled growth rates are for the period 1981 to 1990, whereas the observations are for 1981 to 1995.

rates vary less than the observed rates, but they induce a similar trend in the seasonal cycle. For stations north of 55°N the north of 40°N partition generates an amplitude trend of 0.56% yr^{-1} from 1981 to 1990 in comparison with 0.66% yr^{-1} for the NOAA/CMDL observations from 1981 to 1995).

4. Discussion

4.1. Trends in NOAA/CMDL Flask Station Network

With the inclusion of CO_2 data through December 1995 our analysis supports and strengthens the finding of previous studies that the amplitude of the seasonal cycle is increasing at Arctic and subarctic monitoring stations [*Manning*, 1993; *Conway et al.*, 1994; *Keeling et al.*, 1996]. All five of the NOAA/CMDL stations north of 55°N that have time series extending for 10 or more years have low interannual growth rates during summer months (Figures 6 and 7). Combining all of the data from these stations, we estimate an amplitude trend of 0.66% yr^{-1} ($p \leq 0.01$) for the period from 1981 to 1995.

Comparisons between trends observed here and the trends obtained from other studies is confounded by differences in sampling period, CO_2 data and numerical techniques. At Point Barrow the amplitude increase we calculate (0.45% yr^{-1} from 1971 to 1995) is much lower than the 1.2% yr^{-1} estimate of *Keeling et al.* [1996] for the period 1961 to 1994. Much of this difference may be the result of the difference in sampling period. *Keeling et al.* [1996] include data from 1961 to 1967 in their analysis, whereas in the NOAA/CMDL record begins in 1971. The amplitudes for the period 1961 to 1967 are smaller than those observed after 1973 (Figure 2 of *Keeling et al.* [1996]).

Outside the Arctic, Mauna Loa is the only station in the northern hemisphere with a significant amplitude trend. The 0.69% yr^{-1} increase in the amplitude at Mauna Loa calculated here for the period of 1976 to 1995 is similar to the 0.67% yr^{-1} estimate obtained by *Keeling et al.* [1996] for the period 1958 to 1994 and the 0.70% yr^{-1} estimate obtained by *Bacastow et al.* [1985] for the period 1958 to 1982.

4.2. Footprints of Terrestrial Ecosystems at Observation Stations

The contribution of fossil fuel, biomass burning, ocean, and terrestrial biosphere NEP fluxes to seasonal variation at observation stations has been well characterized with the use of three-dimensional atmospheric tracer transport models [*Heimann et al.*, 1986; *Iacobellis et al.*, 1994; *Denning*, 1994; *Hunt et al.*, 1996; *Erickson et al.*, 1996]. What is unique here is our extensive spatial subdivision of fluxes from the terrestrial biosphere and our analysis of their individual impact on various observation stations using the CASA and GISS models. The results presented in Tables 4, 5, and 6 suggest that the seasonal cycle at Mauna Loa and at other surface observation stations in the northern hemisphere reflects primarily fluxes from high-latitude ecosystems (e.g., tundra, boreal forest, and mixed deciduous forest), and it follows that interannual variation in NEP fluxes from these regions will have a disproportionate effect on anomalies at observation stations. The impact of these regions is even more striking given their relatively minor contribution to global NPP (Table 3). For example, ecosystems north of 40°N have an NPP of only 12.9 Pg C yr^{-1} (23% of a global NPP of 54.9 Pg C yr^{-1}), yet they are the dominant contributor to the seasonal cycle at all of the stations examined here in the northern hemisphere and at several stations in the southern hemisphere.

The disproportionate impact of high-latitude ecosystems on the seasonal cycle of surface observation stations is consistent with results obtained by *Nemry et al.* [1996], using a Fourier analysis approach, and by *Kaminski et al.* [1996], using an adjoint to a tracer transport model. While both of these two footprint studies used the TM2 tracer transport model, estimates of NEP were obtained by using different terrestrial biosphere models. NEP in the study of *Nemry et al.* [1996] was generated by using the Carbon Assimilation in the Biosphere (CARAIB) model, while *Kaminski et al.* [1996] used the Simple Diagnostic Biosphere Model (SDBM) developed by *Knorr and Heimann* [1995]. Examining just the contribution of boreal forests, *D'Arrigo et al.* [1987] found that over 50% of the seasonal amplitude at Barrow and 30% at Mauna Loa could be explained by NEP from this biome.

In contrast to high-latitude ecosystems, tropical forests have a relatively small impact on middle- and high-latitude observation stations. The different effect of high-latitude and tropical ecosystems on the seasonal cycle of CO_2 concentrations at observation stations can be at least partially explained by broad patterns of atmospheric circulation. Equatorial advective transport near the surface and strong vertical convection in tropical regions [*Plumb and*

McConalogue, 1988] minimize the influence of low latitude surface fluxes on the seasonal cycle of CO_2 at poleward observation stations. Vertical convection also acts as a barrier to the movement of gaseous species across hemispheres, thus reducing the contribution of southern hemisphere biomes to the seasonal cycle of CO_2 at stations in the northern hemisphere.

4.3. Impacts of Anthropogenic Forcing on Trends in the Seasonal Cycle

4.3.1. Biomass burning. Biomass burning fluxes contribute substantially to the seasonal cycle in the southern hemisphere (Table 4). Our results are consistent with several recent studies demonstrating the importance of including this tracer in reconstructing CO_2 observations in the tropics and in the southern hemisphere [*Iacobellis et al.*, 1994; *Hunt et al.*, 1996; *Erickson et al.*, 1996].

4.3.2. Fossil fuel emissions. Our analysis of the contribution of fossil fuel emissions to trends in the seasonal cycle is based on a time series of emissions that varies seasonally and geographically from 1958 to 1990 in a manner consistent with known constraints [*Andres et al.*, 1996; *Boden et al.*, 1995; *Rotty*, 1987]. We considered the impacts of this tracer at 19 stations from Alert to South Pole and find that (1) in the northern hemisphere the effects of fossil fuels are pervasive and varying, and at Mauna Loa, approximately 25% of the measured trend can be explained by fossil fuels; (2) the contribution of fossil fuels to trends in the seasonal cycle at high-latitude stations in the northern hemisphere appears to decrease during the 1980s as emission rates from high-latitude regions of the northern hemisphere stabilized; and (3) in the southern hemisphere, CO_2 measurements at Seychelles, Ascension, and Samoa Islands show an extreme sensitivity to changes in fossil fuel emissions. This sensitivity may result from the seasonal movement of the ITCZ, periodically bringing CO_2-enriched northern hemisphere air into contact with the low-latitude observation stations.

Previous analyses using an earlier version of the GISS model found that almost 50% of the trend at Mauna Loa could be explained by fossil fuels [*Heimann et al.*, 1986]. When winds derived from the Global Weather Experiment were used to drive a similar tracer model, however, the contribution of fossil fuels to the Mauna Loa signal was found to be negligible [*Heimann et al.*, 1989]. The discrepancy between these two estimates has been attributed to differences in the wind fields. The earlier version of the GISS model, driven by winds derived from an 8° x 10° GCM, may have overestimated the strength and movement of the ITCZ. Here the GISS tracer model included corrections for horizontal diffusion associated with large-scale convective events and was driven by winds derived from a 4° x 5° GCM. With these improvements we predict a fossil-fuel-induced trend approximately halfway between the two previous estimates of *Heimann et al.* [1986] and *Heimann et al.* [1989].

The wide variation among model estimates of the fossil fuel-induced trend suggests that other tracer models need to be employed to address this question. Both the GISS model used here and the tracer model employed by *Heimann and Keeling* [1989] lack a variable height planetary boundary layer (PBL) [e.g., *Denning*, 1994]. Vertical mixing by PBL turbulence can enhance the seasonal variation of surface CO_2 concentrations that is driven by the covariance of seasonal NEP with meridional transport and convective mixing [*Denning et al.*, 1995].

The seasonal cycle of emissions that we superimposed on the fossil fuel time series was representative of conditions in 1982. Over the period of our analyses, from 1961 to 1990, we expect that the actual seasonality diminished. The fraction of total emissions arising from the consumption of gas and solids (components most frequently used for heating) decreased from 62% in 1960 to 56% in 1990 [*Boden et al.*, 1995]. Emissions from the consumption of liquid fuels went up proportionally. However, the overall impact of this change in the seasonality has probably only a minor effect on our results. Estimated trends are more likely to be sensitive to model representations of atmospheric circulation [e.g., *Law et al.*, 1996], as discussed above.

Some uncertainty, however, appears to exist in the magnitude of seasonal variation predicted by *Rotty* [1987]. Atmospheric measurements of $^{14}CO_2$ suggest that the seasonal cycle of fossil fuel emissions is more than 3 times greater than the *Rotty* [1987] estimates for northern Europe [*Levin et al.*, 1995]. *Levin et al.* [1995] propose that this discrepancy may arise from differences in the times fossil fuels are purchased (i.e., the basis for the *Rotty* [1987] estimates) and the times they are actually consumed. Increasing the seasonal cycle of fossil fuel emissions in the GISS tracer model or in other tracer models by a factor of 3 may lead to substantially higher estimates of the impacts of fossil fuel emissions on trends in the seasonal cycle.

4.3.3. NPP stimulation. Fertilization from increasing concentrations of atmospheric CO_2 and nitrogen deposition are proposed to account for a large fraction of the terrestrial sink [*Mellilo et al.*, 1996; *Schimel et al.*, 1995]. Both of these mechanisms require year-to-year increases in NPP that must occur each season as a set of incremental changes in monthly NPP. In the NPP stimulation runs presented here we assumed that the seasonal distribution of NPP increase is proportional to the steady state seasonal cycle of NPP. In section 2.3.3 we argue that this seasonal distribution is consistent with CO_2 and nitrogen fertilization. In the context of NPP stimulation playing an important role in terrestrial uptake, here we consider links between the amplitude increases and the latitudinal distribution of terrestrial uptake.

If the total magnitude of the terrestrial sink is known from other constraints (e.g., from ^{13}C, the meridional gradient of CO_2, or the O_2/N_2 ratio), then the high-latitude amplitude observations in the northern hemisphere provide an additional constraint on the geographic distribution of uptake. To satisfy observed amplitude increases at Arctic and subarctic stations and a terrestrial sink of 1.9 Pg C yr^{-1} for the 1980s [*Schimel et al.*, 1995], then most of the NPP increases and thus the sink need to be distributed north of 30°N (Table 7, Figure 12). If NPP increases associated with a 1.9 Pg C yr^{-1} terrestrial sink were confined to regions south of 30°N, the resulting NEP fluxes would leave no detectable impact on the seasonal cycle of CO_2 at Arctic and subartic observation stations and would create an untenably large sink inconsistent with independent estimates (Table 8, Figure 12).

This result is consistent with constraints on the location of the sink from ^{13}C [*Ciais et al.*, 1995] and ocean pCO_2 [*Tans et al.*, 1990] that place a significant fraction of the terrestrial sink at midlatitudes in the northern hemisphere. Both of these studies, however, leave open the possibility of a high-latitude terrestrial source. The results of *Ciais et al.* [1995] show a terrestrial release of CO_2 north of 60°N. In scenarios 6, 7, and 8 of *Tans et al.* [1990] the meridional gradient of CO_2 was reproduced with a boreal source of 0.2 to 0.7 Pg C yr^{-1}. A simple explanation for the high-latitude amplitude increases and a 1.9 Pg C yr^{-1} terrestrial sink is that large increases in NPP occur continuously from the Arctic to midlatitudes in the northern hemisphere. If there is a small high-latitude terrestrial source, the amplitude observations suggest that it is offset by large terrestrial NPP increases just to the south.

An important limitation of this study with respect to confining the geographic distribution of a terrestrial sink is that in CASA, forest NPP does not depend on stand age. A terrestrial sink associated with forest regrowth could occur even though NPP might be declining in mature forests. The decreases in NPP could lead in turn to decreases in the amplitude of the seasonal cycle. In CASA these would require even larger increases in NPP in other regions to match the amplitude observations. The trends in the seasonal cycle that are driven by forest regrowth can be assessed by models that include forest demography [e.g., *Kohlmaier et al.*, 1995; *Murty et al.*, 1996; *Kurz et al.*, 1992]. By identifying the signature of forest regrowth on changes in the seasonal cycle of NEP these models could be used in conjunction with the trend observations to provide additional constraints on the fraction of the total terrestrial sink that is driven by forest regrowth.

4.4. What Is the Contribution of CO_2 Fertilization to the Terrestrial Sink?

To match the historical sink estimate of *Houghton* [1995] with the CASA model, large increases in NPP are required. *Thompson et al.* [1996] showed that a cumulative increase in NPP of 20% from 1880 to 1990 was required to match the *Houghton* [1995] estimate when NPP increases were distributed evenly over all terrestrial areas. The linear β factor for CO_2 fertilization that corresponds to this NPP increase is 0.9 [*Thompson et al.*, 1996], approximately 3 times higher than the mean β factor reported in CO_2 enrichment studies [*Amthor and Koch*, 1996]. However, we find that amplitude increases generated from this run are half or less those observed at Arctic and subarctic stations north of 55°N and at Mauna Loa (Figure 10). Thus to match the amplitude observations, we require that NPP increase even faster than it does in the study of *Thompson et al.* [1996], such that it drives a terrestrial sink two to three times the *Houghton* [1995] estimate. For the period of 1961 to 1990 this amounts to a 0.5% to 0.8% yr^{-1} increase in NPP. As we discussed in section 4.3, such NPP increases are compatible with independent sink estimates only when they are confined to regions north of 30°N or 40°N. The corresponding β values necessary under these constraints range between 1.5 and 2.4, 4 to 6 times greater than the mean of the experimental values.

An intriguing interpretation of this result is that for a given terrestrial sink, only a small fraction of it is driven by CO_2 fertilization. Other studies examining perturbations in NPP required to match the amplitude increase have also found it unrealistic to ascribe all of the response to CO_2 fertilization. For a deciduous forest in the northeastern United States, *Houghton* [1987] found that a modeled β factor of 1.1 was required to match the amplitude increases. Using a realistic β of 0.4, *Kohlmaier et al.* [1989] estimated that CO_2 fertilization in the northern hemisphere could account for only a 0.15% yr^{-1} increase in the amplitude at Mauna Loa, or 22% of the observed signal. *Bonan* [1992] found that a small and probably undetectable change in aboveground biomass was required to create 0.5% yr^{-1} amplitude increases in the seasonal cycle of fluxes in a boreal forest model. Again, the β factor that corresponds to the reported NPP stimulation in Bonan's study is very high (2.2).

Nitrogen fertilization in high-latitude ecosystems could account for at least some of the rapid NPP increases required to explain the seasonal amplitude increases. Nitrogen deposition originating from industrial centers in Europe, North America and Asia is the highest in the northern hemisphere between 30°N and 60°N with a peak at 50°N [*Holland et al.*, 1997; *Townsend et al.*, 1996]. The corresponding meridional distribution of carbon uptake predicted by *Holland et al.* [1997] agrees well with the distribution of NPP increases and subsequent terrestrial uptake that we find necessary to match the amplitude observations at high-latitudes. Other possible explanations for the disparity between experimental β's and those required for consistency with the amplitude increases include: (1) that β was much higher from 330 - 360 ppm than from 360 - 700 ppm (perhaps resulting from the greater sensitivity of photosynthesis to CO_2 at lower atmospheric concentrations [*Amthor and Koch*, 1996]); and (2) other ecosystem processes besides NPP stimulation are driving a large part of the amplitude increases.

4.5. Is there a Point Barrow-Mauna Loa Gradient in the Amplitude Trend?

There is some evidence for a gradient in amplitude increase for stations in the northern hemisphere. Within the Arctic, amplitude trends fall off quickly for stations closer to the equator (Table 1). *Keeling et al.* [1996] showed greater amplitude increases at Point Barrow than at Mauna Loa. Fossil-fuel-induced amplitude increases are likely to comprise a larger fraction of the total trend for Mauna Loa than for stations north of 55°N (Figure 9, Table 7). If the modeled fossil fuel trends were subtracted from the observed trends, the difference between Barrow and Mauna Loa would be even greater.

In consideration of the reversal of the Arctic seasonal pattern of interannual growth rates observed at Shemya, Cape Meares, and Niwot Ridge it appears that available CO_2 time series are of insufficient length to conclusively resolve such a gradient. Nonetheless, the possibility is an interesting one to explore in the context of the NPP stimulation runs presented here. None of the model runs with spatially uniform NPP increases produced a meridional gradient in amplitude trends in the northern hemisphere (Figure 10). To explain such a gradient with CASA and the GISS models, the NPP increases would have to be confined to regions north of 50°N, or even 60°N (Figure 12). Tundra contributes 3 times as much to the

mean seasonal cycle at Point Barrow as it does at Mauna Loa (Table 4). Thus, if NPP increases were confined to tundra regions, the Barrow amplitude would increase 3 times faster than the amplitude at Mauna Loa, consistent with the data from *Keeling et al.* [1996].

4.6. Modeled and Observed Zero Crossing Times

We compared modeled and observed changes in the zero crossing time for stations north of 55°N, and we find that the rate of change of the zero crossing time from the 3 x Ho partition north of 40°N advanced at a rate of 2.59 days per decade for the period 1981 to 1990. This value closely matches the 2.48 days per decade observed in the NOAA/CMDL record for the same set of stations from 1981 to 1995 (section 3.1).

For Barrow and the other Arctic stations the zero crossing time occurs near the end of June (Julian day 180). Even if CO_2 concentrations in June remained constant, a decrease in concentrations during July (from greater ecosystem uptake) would cause the zero crossing time to advance. In the NPP stimulation runs using CASA we imposed NPP increases in proportion to the steady state seasonal cycle of NPP. For high-latitude ecosystems, most of the NPP increases occurred later than June (the seasonal cycle of NPP closely follows the seasonal cycle of APAR shown in Figure 1), but nevertheless, our modeled zero crossing times are comparable with the observations. Thus, in contrast to *Keeling et al.* [1996], we find that an advance in the zero crossing does not necessarily imply an extension of the growing season.

4.7. Interannual Growth Rate Signatures of Terrestrial Sources and Sinks

The amplitude trend (equation (2)) is one index of change in the seasonal cycle. This index uses interannual CO_2 growth rates only during months of maximum and minimum CO_2 concentrations. Growth rates during other months are not considered, even though they provide continuity between the extremes. Patterns of seasonal variation in growth rates extend across groups of stations that experience similar air masses (Figure 6).

The seasonal pattern of interannual growth rates could provide additional constraints on the distribution of terrestrial sources and sinks. Each terrestrial source and sink may have its own distinctive spatio-temporal signature. Linear combinations of sink and source growth rate end-members that match observations may allow partitioning among different source/sink components. For example, the fossil fuel source produces an end-member that is easily distinguishable in magnitude and shape from the one produced by the NPP increases (Figure 13). In the case of uptake by the terrestrial biosphere this approach may provide clues to the seasonal timing of NPP increases. For the Arctic and subarctic stations analyzed here, our model estimates of detrended CO_2 concentrations are almost perfectly in phase with the observations (Figure 8, Table 4). Yet the interannual CO_2 growth rates that we predict from NPP stimulation lag behind the observations by 2 months (Figure 13).

One particularly interesting direction for future study is to confine NPP increases to different seasons to improve the match between modeled and observed seasonal variation in interannual growth rates. If, for example, terrestrial NPP increases were confined to spring months [e.g., *Keeling et al.*, 1996], could we eliminate the phase lag? Conversely, if NPP increases were confined to periods near the end of the growing season, would the fit between modeled and observed growth rates worsen? An analysis of modeled and observed seasonal variation in interannual growth rates provides a new approach for testing the growing season hypothesis proposed by *Keeling et al.* [1996].

4.8. Uncertainties in Our Understanding of the Seasonal Cycle of CO_2

By using the same set of winds each year, from 1958 to 1990, we were able to identify the contribution of changes in terrestrial surface sources and sinks to trends in the seasonal cycle. Year-to-year variation in transport, however, is substantial and is clearly a source of the variability in CO_2 observations. A systematic change in transport over the last several decades could induce a trend in the seasonal cycle. At regional scales, human transformation of the land surface during this period has been substantial. Human-induced changes in surface roughness, albedo, and leaf area have the potential to change humidity, wind speed, PBL height and the general circulation of the atmosphere [*Chase et al.*, 1996; *Copeland et al.*, 1996]. While such effects may be minimal at observation stations that sample primarily marine air, they cannot be dismissed as contributing factors to the observed trends in the seasonal cycle.

From the footprint analysis (Table 5) it appears that all stations are influenced to some degree by agriculture. In addition to their potential impacts on atmospheric transport as described above, agricultural regions have undergone profound changes in carbon and nutrient cycling. Many areas are depleted in soil carbon [*Tiessen et al.*, 1994], making heterotrophic respiration sensitive to changes in the size of labile litter fractions [*Randerson et al.*, 1996]. The total impact of agriculture on trends in the seasonal cycle is difficult to estimate, however, because of our limited understanding of how surface fluxes have changed in these regions over the last few decades.

At high latitudes in the northern hemisphere, temperatures during the spring and winter increased from 1961 to 1990 [*Chapman and Walsh*, 1993]. These observations provide the basis for *Keeling et al.*'s [1996] hypothesis that temperature increases have driven an increase in growing season length over this same period. The possibility, however, of a more direct connection between temperature increases and the amplitude trends cannot be dismissed. For example, it is possible that long term changes in atmospheric transport in the Arctic are directly causing the increasing temperatures. The changes in atmospheric transport could also change the footprint of observation stations, thus inducing a trend in the seasonal cycle, independent of any changes in NPP or any other aspect of ecosystem function.

In general, the observed pattern of high winter growth rates and low summer growth rates at Arctic stations are not as persistent further south, as we would predict if NPP increases associated with a northern hemisphere terrestrial sink were driving the trends at stations north of 55°N. In particular, the high summer growth rates observed for Shemya, Cape Meares,

and Niwot Ridge are not captured by our model simulations, suggesting that there may be other processes at work in shaping trends in the seasonal cycle that are not represented here.

5. Conclusions

Direct anthropogenic forcing of the seasonal cycle in the southern hemisphere from fossil fuel combustion and biomass burning makes it unlikely that trends in the seasonal cycle of CO_2 from stations in the southern hemisphere can be used to constrain interannual changes in carbon fluxes from terrestrial ecosystems. In contrast, for Arctic and subarctic stations in the northern hemisphere, fossil fuel emissions and tropical biomass burning appear to have little impact on trends in the seasonal cycle of CO_2. This finding suggests that the observed trends at high latitudes can be attributed to processes almost solely within terrestrial ecosystems, in particular, within tundra and boreal forest biomes.

We find that large NPP increases would be required to explain the amplitude observations at Arctic and subarctic stations in the northern hemisphere. The high rates of NPP increase are incompatible with CO_2 fertilization playing the dominant role in driving the trends in the seasonal cycle. Our results support several previous studies that have reached similar conclusions [*Houghton*, 1987; *Kohlmaier et al.*, 1989]. Thus it is likely that other processes in middle- and high-latitude terrestrial ecosystems in the northern hemisphere, including NPP stimulation by nitrogen deposition, are responsible for the observed trends. NPP stimulation by nitrogen deposition would also lead to a northern hemisphere terrestrial sink consistent with other constraints from ^{13}C and the annual meridional gradient of CO_2.

Acknowledgments. We wish to thank R. Andres for providing the fossil fuel maps, W. M. Hao for providing the biomass burning data, and J. John for assistance with the GISS tracer model. J. A. Berry, C. M. Malmstrom, J. F. Polsenberg, C. J. Still, P. M. Vitousek, and three anonymous reviewers provided very helpful suggestions. This work was supported in part by a NASA EOS/IDS grant to P. J. Sellers and H. A. Mooney and a grant to C.B.F. and J. A. Berry from the Western Regional Center of the DOE National Institute for Global Environmental Change. J.T.R. was supported by a NASA Earth System Science Graduate Fellowship. The Pathfinder NDVI data were acquired from the Distributed Active Archive Center (code 902.2) at the Goddard Space Flight Center, Greenbelt, Maryland. The maps of NEP fluxes and the CASA computer code used in this study are available via anonymous ftp at arbutus.stanford.edu in the directory pub/amp. This is CIW-DPB publication 1324.

References

Amthor, J.S., and G.W. Koch, Biotic growth factor β: Stimulation of terrestrial ecosystem net primary productivity by elevated atmospheric CO_2, in *Carbon Dioxide and Terrestrial Ecosystems*, edited by G.W. Koch and H.A. Mooney, pp. 399-414, Academic, San Diego, Calif., 1996.

Andres, R.J., G. Marland, I.Y. Fung, and E. Matthews, A 1° x 1° distribution of carbon dioxide emissions from fossil fuel consumption and cement manufacture, 1950-1990, *Global Biogeochem. Cycles*, *10*(3), 419-430, 1996.

Bacastow, R.B., C.D. Keeling, and T.P. Whorf, Seasonal amplitude increase in atmospheric CO_2 concentration at Mauna Loa, Hawaii, 1959-1982, *J.Geophy. Res.*, *90*(D6), 10,529-10,540, 1985.

Baker, C.B., T.R. Eischeid, T.R. Karl, and H.F. Diaz, The quality control of long-term climatological data using objective data analysis, paper presented at Ninth Conference on Applied Climatology, Am. Meteorol. Soc., Dallas, Tex., 1995.

Bishop, J.K.B., and W.B. Rossow, Spatial and temporal variability of global surface solar irradiance, *J. Geophys. Res.*, *96*(C9), 16,839-16,858, 1991.

Boden, T., G. Marland, and B. Andres, Estimates of global, regional, and national annual CO_2-emissions from fossil-fuel burning, hydraulic cement production and gas flaring: 1950:1992, report, Carbon Dioxide Inf. and Anal. Cent., Oak Ridge Nat. Lab., Oak Ridge, Tenn., 1995.

Bonan, G.B., Comparison of atmospheric CO_2 concentration and metabolic activity in boreal forest ecosystems, *Tellus, Ser. B*, *44*, 173-185, 1992.

Bruno, M., and F. Joos, Terrestrial carbon storage during the past 200 years: A Monte Carlo analysis of CO_2 data from ice core and atmospheric measurements, *Global Biogeochem. Cycles*, *11*(1), 111-124, 1997.

Chan, Y.-H., and C.S. Wong, Long-term changes in amplitudes of atmospheric CO_2 concentrations at Ocean Station P and Alert, Canada, *Tellus, Ser. B*, *42*, 330-341, 1990.

Chapman, W.L., and J.E. Walsh, Recent variations of sea ice and air temperatures in high latitudes, *Bull. Am. Meteorol. Soc.*, *74*(1), 33-47, 1993.

Chase, T.N., R.A. Pielke, T.G.F. Kittel, R. Nemani, and S.W. Running, Sensitivity of a general circulation model to changes in leaf area index, *J. Geophys. Res.*, *101*(D3), 7393-7408, 1996.

Ciais, P., P.P. Tans, M. Trolier, J.W.C. White, and R.J. Francey, A large northern hemisphere terrestrial CO_2 sink indicated by the $^{13}C/^{12}C$ ratio of atmospheric CO_2, *Science*, *269*, 1098-1102, 1995.

Cleveland, R.B., W.S. Cleveland, J.E. McRae, and I. Terpenning, STL: A seasonal-trend decomposition procedure based on loess, *J. of Off. Stat.*, *6*(1), 3-73, 1990.

Cleveland, W.S., A.E. Freeny, and T.E. Graedel, The seasonal component of atmospheric CO_2: Information from new approaches to the decomposition of seasonal time series, *J. Geophys. Res.*, *88*(C15), 10,934-10,946, 1983.

Conway, T.J., P.P. Tans, L.S. Waterman, K.W. Thoning, D.R. Kitzis, K.A. Masarie, and N. Zhang, Evidence for interannual variability of the carbon cycle from the National Oceanic and Atmospheric Administration/Climate Monitoring and Diagnostics Laboratory global air sampling network, *J. Geophys. Res.*, *99*(D11), 22,831-22,855, 1994.

Copeland, J.H., R.A. Pielke, and T.G.F. Kittel, Potential climatic impacts of vegetation change: A regional modeling study, *J. Geophys. Res.*, *101*(D3), 7409-7418, 1996.

Crutzen, P.J., and M.O. Andreae, Biomass burning in the tropics: Impacts on atmospheric chemistry and biogeochemical cycles, *Science*, *250*, 1669-1678, 1990.

D'Arrigo, R., G.C. Jacoby, and I.Y. Fung, Boreal forests and atmosphere-biosphere exchange of carbon dioxide, *Nature*, *329*, 321-323, 1987.

DeFries, R.S., and J.R.G. Townshend, NDVI-derived land cover classifications at a global scale, *Int. J. Remote Sens.*, *15*(17), 3567-3586, 1994.

Denning, A.S., Investigations of the transport, sources and sinks of atmospheric CO_2 using a general circulation model, Ph. D. thesis, Colo. State Univ., Fort Collins, 1994.

Denning, A.S., I.Y. Fung, and D. Randall, Latitudinal gradient of atmospheric CO_2 due to seasonal exchange with land biota, *Nature*, *376*, 240-243, 1995.

Erickson, D.J., III, P.J. Rasch, P.P. Tans, P. Friedlingstein, P. Ciais, E. Maier-Reimer, K. Six, C.A. Fischer, and S. Walters, The seasonal cycle of atmospheric CO_2: A study based on the NCAR Community Climate Model (CCM2), *J. Geophys. Res.*, *101*(D10), 15,079-15,097, 1996.

Field, C.B., J.T. Randerson, and C.M. Malmström, Ecosystem net primary production: Combining ecology and remote sensing, *Remote Sens. of Environ.*, *51*(1), 74-88, 1995.

Fung, I., K. Prentice, E. Matthews, J. Lerner, and G. Russell, Three-

dimensional tracer model study of atmospheric CO_2: Response to seasonal exchanges with the terrestrial biosphere, *J. Geophys. Res.*, *88*(C2), 1281-1294, 1983.

Fung, I.Y., J. John, J. Lerner, E. Matthews, M. Prather, L.P. Steele, and P.J. Fraser, Three-dimensional model synthesis of the global methane cycle, *J. Geophys. Res.*, *96*(D7), 13,033-13,065, 1991.

Fung, I.Y., C.J. Tucker, and K.C. Prentice, Application of advanced very high resolution radiometer vegetation index to study atmosphere-biosphere exchange of CO_2, *J. Geophys. Res.*, *92*(D3), 2999-3015, 1987.

Gower, S.T., R.E. McMurtrie, and D. Murty, Aboveground net primary production decline with stand age: potential causes, *Trends Ecol. Evol.*, *11*(9), 378-381, 1996.

Hansen, J., and S. Lebedeff, Global trends of surface air temperature, *J. Geophys. Res.*, *92*(D11), 13,345-13,372, 1987.

Hansen, J., and S. Lebedeff, Global surface air temperatures: Update through 1987, *Geophys. Res. Lett.*, *15*, 323-326, 1988.

Hao, W.M., and M.-H. Liu, Spatial and temporal distribution of biomass burning, *Global Biogeochem. Cycles*, *8*(4), 495-503, 1994.

Hao, W.M., M.-H. Liu, and P.J. Crutzen, Estimates of annual and regional releases of CO_2 and other trace gases to the atmosphere from fires in the tropics based on FAO statistics for the period 1975-1980, in *Fire in the Tropical Biota*, edited by J.G. Goldammer, pp. 440-462, Springer-Verlag, New York, 1990.

Heimann, M., and C.D. Keeling, A three-dimensional model of atmospheric CO_2 transport based on observed winds, 2, Model description and simulated tracer experiments, in *Aspects of Climate Variability in the Pacific and the Western Americas*, *Geophys. Monogr. Ser.*, vol. 55, edited by D.H. Peterson, pp. 237-275, AGU, Washington, D.C., 1989.

Heimann, M., C.D. Keeling, and C.J. Tucker, A three-dimensional model of atmospheric CO_2 transport based on observed winds, 3, Seasonal cycle and synoptic time scale variations, in *Aspects of Climate Variability in the Pacific and the Western Americas*, *Geophys. Monogr. Ser.*, vol. 55, edited by D.H. Peterson, pp. 277-303, AGU, Washington, D.C., 1989.

Heimann, M.M., C.D. Keeling, and I.Y. Fung, Simulating the atmospheric carbon dioxide distribution with a three dimensional tracer model, in *The Changing Carbon Cycle: A Global Analysis*, edited by J.R. Trabalka and D.E. Reichle, pp. 16-49, Springer-Verlag, New York, 1986.

Holland, E.A., B.H. Braswell, J.-F. Lamarque, A. Townsend, J. Sulzman, J.-F. Muller, F. Dentener, G. Brasseur, H.I. Levy, II,, J.E. Penner, and G.-J. Roelofs, Variations in the predicted spatial distribution of atmospheric nitrogen deposition and their impact on carbon uptake by terrestrial ecosystems, *J. Geophys. Res.*, *102*(D13), 15,849-15,866, 1997.

Houghton, R.A., Biotic changes consistent with the increased seasonal amplitude of atmospheric CO_2 concentrations, *J. Geophys. Res.*, *92*(D4), 4223-4230, 1987.

Houghton, R.A., Changes in terrestrial carbon over the last 135 years, in *The Global Carbon Cycle*, edited by M. Heimann, Springer-Verlag, New York, 1993.

Houghton, R.A., Effects of land-use change, surface temperature, and CO_2 concentration on terrestrial stores of carbon, in *Biotic Feedbacks in the Global Climate System: Will the Warming Feed the Warming?*, edited by G.M. Woodwell and F.T. MacKenzie, pp. 334-350, Oxford Univ. Press, New York, 1995.

Houghton, R.A., and J.L. Hackler, The net flux of carbon from deforestation and degradation in south and southeast Asia, in *Effects of Land-Use Change on Atmospheric CO_2 Concentrations: South and Southeast Asia as a Case Study*, edited by V.H. Dale, pp. 301-328, Springer-Verlag, New York, 1994.

Hunt, E.R.J., S.C. Piper, R. Nemani, C.D. Keeling, R. Otto, and S.W. Running, Global net carbon exchange and intra-annual CO_2 concentrations predicted by an ecosystem process model and a three-dimensional atmospheric transport model, *Global Biogeochem. Cycles*, *10*(3), 431-456, 1996.

Iacobellis, S.F., R. Frouin, H. Razafimpanilo, R.C.J. Somerville, and S.C. Piper, North African savanna fires and atmospheric CO_2, *J. Geophys. Res.*, *99*(D4), 8321-8334, 1994.

Kaminski, T., R. Giering, and M. Heimann, Sensitivity of the seasonal cycle of CO_2 at remote monitoring stations with respect to seasonal surface exchange fluxes determined with the adjoint of an atmospheric transport model, in *Phys. Chem. Earth*, 21, 457-462, 1996.

Keeling, C.D., R.B. Bacastow, A.F. Carter, S.C. Piper, T.P. Whorf, M. Heimann, W.G. Mook, and H. Roeloffzen, A three-dimensional model of atmospheric CO_2 transport based on observed winds, 1, Analysis of observational data, in *Aspects of Climate Variability in the Pacific and the Western Americas*, *Geophys. Monogr. Ser.*, vol. 55, edited by D.H. Peterson, pp. 165-236, AGU, Washington, D.C., 1989a.

Keeling, C.D., S.C. Piper, and M. Heimann, A three-dimensional model of atmospheric CO_2 transport based on observed winds, 4, Mean annual gradients and interannual variations, in *Aspects of Climate Variability in the Pacific and the Western Americas*, *Geophys. Monogr. Ser.*, vol. 55, edited by D.H. Peterson, pp. 305-365, AGU, Washington, D.C., 1989b.

Keeling, C.D., J.F.S. Chin, and T.P. Whorf, Increased activity of northern vegetation inferred from atmospheric CO_2 observations, *Nature*, *382*, 146-149, 1996.

Knorr, W., and M. Heimann, Impact of drought stress and other factors on seasonal land biosphere CO_2 exchange studied through an atmospheric tracer transport model, *Tellus*, *Ser. B*, *47*, 471-489, 1995.

Kohlmaier, G.H., E.O. Sire, A. Janecek, C.D. Keeling, S.C. Piper, and R. Revelle, Modeling the seasonal contribution of a CO_2 fertilization effect of the terrestrial vegetation to the amplitude increase in atmospheric CO_2 at Mauna Loa observatory., *Tellus*, *Ser. B*, *41*, 487-510, 1989.

Kohlmaier, G.H., C. Hager, G. Wurth, M.K.B. Ludecke, P. Ramge, F.-W. Badeck, J. Kindermann, and T. Lang, Effects of the age class distribution of the temperate and boreal forests on the global CO_2 source-sink function, *Tellus*, *Ser. B*, *47*, 212-231, 1995.

Kurz, W.A., M.J. Apps, T.M. Webb, and P.J. McNamee, *The Carbon Budget of the Canadian Forest Sector: Phase 1*, 93 pp., For. Canada, Northwest Region, Northwest For. Cent., Edmonton, Alberta, 1992.

Law, R.M., et al., Variations in modeled atmospheric transport of carbon dioxide and the consequences for CO_2 inversions, *Global Biogeochem. Cycles*, *10*(4), 783-796, 1996.

Lerner, J.E., E. Matthews, and I.Y. Fung, Methane emissions from animals: A global high-resolution database, *Global Biogeochem. Cycles*, *2*(2), 139-156, 1988.

Levin, I., R. Graul, and N.B.A. Trivett, Long-term observations of atmospheric CO_2 and carbon isotopes at continental sites in Germany, *Tellus*, *Ser. B*, *47*, 23-34, 1995.

Los, S.O., C.O. Justice, and C.J. Tucker, A global 1° x 1° NDVI data set for climate studies derived from GIMMS continental NDVI data, *Int. J. Remote Sens.*, *15*(17), 3493-3518, 1994.

Manning, M.R., Seasonal cycle in atmospheric CO_2 concentrations, in *The Global Carbon Cycle*, edited by M. Heimann, pp. 65-93, Springer-Verlag, New York, 1993.

Matthews, E., Global vegetation and land use: New high-resolution data bases for climate studies, *J. Clim. Applied Meteorol.*, *22*, 474-487, 1983.

Melillo, J.M., I.C. Prentice, G.D. Farquhar, E.-D. Schultze, and O.E. Sala, Terrestrial biotic responses to environmental change and feedbacks to climate, in *Climate Change 1995: The Science of Climate Change Contribution of Working Group 1 to the Second Assessment Report of the Intergovernmental Panel on Climate Change*, edited by B. Bolin, J.T. Houghton, and L.G. Meira Filho, pp. 445-481, Cambridge Univ. Press, New York, 1996.

Murty, D., R.E. McMutrie, and M.G. Ryan, Declining forest productivity in aging forest stands: a modeling analysis of alternative hypotheses, *Tree Physiol.*, *16*, 187-200, 1996.

Myneni, R.B., C.D. Keeling, C.J. Tucker, G. Asrar, and R.R. Nemani, Increased plant growth in the northern high latitudes from 1981-1991, *Nature*, *386*, 698-702, 1997.

Nemry, B., L. Francois, P. Warnant, F. Robinet, and J.-C. Gerard, The seasonality of the CO_2 exchange between the atmosphere and the land biosphere: A study with a global mechanistic vegetation model, *J. Geophys. Res.*, *101*(D3), 7111-7125, 1996.

Parton, W.J., et al., Observations and modeling of biomass and soil organic matter dynamics for the grassland biome worldwide, *Global Biogeochem. Cycles*, *7*(4), 785-809, 1993.

Pearman, G.I., and P. Hyson, The annual variation of atmospheric CO_2 concentration observed in the northern hemisphere, *J. Geophys. Res.*, *86*(C10), 9839-9843, 1981.

Plumb, R.A., and D.D. McConalogue, On the meridional structure of long-lived tropospheric constituents, *J. Geophys. Res.*, *93*(D12), 15,897-15,913, 1988.

Potter, C.S., J.T. Randerson, C.B. Field, P.A. Matson, P.M. Vitousek, H.A. Mooney, and S.A. Klooster, Terrestrial ecosystem production: A process model based on global satellite and surface data, *Global Biogeochem. Cycles*, *7*(4), 811-841, 1993.

Prather, M., M. McElroy, S. Wofsy, G. Russell, and D. Rind, Chemistry of the global troposphere: Fluorocarbons as tracers of air motion, *J. Geophys. Res.*, *92*(D6), 6579-6613, 1987.

Press, W.H., B.P. Flannery, S.A. Teukolsky, and W.T. Vetterling, *Numerical Recipes in C: The Art of Scientific Computing*, Cambridge Univ. Press, New York, 1988.

Raich, J.W., and C.S. Potter, Global patterns of carbon dioxide emissions from soils, *Global Biogeochem. cycles*, *9*(1), 23-36, 1995.

Randerson, J.T., M.V. Thompson, C.M. Malmstrom, C.B. Field, and I.Y. Fung, Substrate limitations for heterotrophs: Implications for models that estimate the seasonal cycle of atmospheric CO_2, *Global Biogeochem. Cycles*, *10*(4), *585-602*, 1996.

Rotty, R.M., Estimates of seasonal variation in fossil fuel CO_2 emissions, *Tellus, Ser. B, 39,* 184-202, 1987.

Russell, G.L., and J.A. Lerner, A new finite differencing scheme for the tracer transport equation, *J. of Appl. Meteorol.*, *20*, 1483-1498, 1981.

Sarmiento, J.L., J.C. Orr, and U. Siegenthaler, A perturbation simulation of CO_2 uptake in an ocean general circulation model, *J. Geophys. Res.*, *97*(3), 3621-3645, 1992.

Schimel, D.S., I.G. Enting, M. Heimann, T.M.L. Wigley, D. Raynaud, D. Alves, and U. Siegenthaler, CO_2 and the carbon cycle, in *Climate Change 1994: Radiative Forcing of Climate Change and an Evaluation of IPCC IS92 Emission Scenarios*, edited by J.T. Houghton, et al., pp. 35-71, Cambridge Univ. Press, New York, 1995.

Sellers, P.J., C.J. Tucker, G.J. Collatz, S.O. Los, C.O. Justice, D.A. Dazlich, and D.A. Randall, A global 1° by 1° NDVI data set for climate studies, 2, The generation of global fields of terrestrial biophysical parameters from the NDVI, *Int. J. Remote Sens.*, *15*(7), 3519-3545, 1994.

Shea, D.J., Climatological atlas: 1950-1979, *Technical Note NCAR TN-269+STR*, Nat. Cent. for Atmos. Res., Boulder, Colo., 1986.

Sokal, R.R., and F.J. Rohlf, *Biometry*, 859 pp., W. H. Freeman, New York, 1980.

Tans, P.P., I.Y. Fung, and T. Takahashi, Observation constraints on the global atmospheric CO_2 budget, *Science*, *247*, 1431-1438, 1990.

Thompson, M.V., J.T. Randerson, C.M. Malmstrom, and C.B. Field, Change in net primary production and heterotrophic respiration: How much is necessary to sustain the terrestrial carbon sink?, *Global Biogeochem. Cycles*, *10*(4), 711-726, 1996.

Thoning, K.W., P.P. Tans, and W.D. Komhyr, Atmospheric carbon dioxide at Mauna Loa observatory, 2, Analysis of the NOAA GMCC data 1974-1985, *J. Geophys. Res.*, *94*(D6), 8549-8565, 1989.

Tiessen, H., E. Cuevas, and P. Chacon, The role of soil organic matter in sustaining soil fertility, *Nature*, *371*, 783-785, 1994.

Townsend, A.R., B.H. Braswell, E.A. Holland, and J.E. Penner, Spatial and temporal patterns in terrestrial carbon storage due to deposition of fossil fuel nitrogen, *Ecol. Appl.*, *6*(3), 806-814, 1996.

Tucker, C.J., I.Y. Fung, C.D. Keeling, and R.H. Gammon, Relationship between atmospheric CO_2 variations and a satellite-derived vegetation index, *Nature*, *319*, 195-199, 1986.

Zobler, L.A., World soil file for global climate modeling, *NASA Tech. Memo.*, *87802*, 32 pp., 1986.

T. J. Conway, Climate Monitoring and Diagnostics Laboratory, National Oceanic and Atmospheric Administration, Boulder, CO 80303. (email: tconway@cmdl.noaa.gov)

C. B. Field and J. T. Randerson, Carnegie Institution of Washington, Department of Plant Biology, Stanford, CA 94305. (email: chris@jasper.stanford.edu; jimr@jasper.stanford.edu)

I. Y. Fung, School of Earth and Ocean Sciences, University of Victoria, P.O. Box 1700, Victoria, British Columbia, Canada V8W 2Y2. (e-mail: inez@garryoak.seaoar.uvic.ca)

M.V. Thompson, Department of Organismic and Evolutionary Biology, Harvard University, Cambridge, MA 02138. (email: mthompso@oeb.harvard.edu)

(Received October 22, 1996; revised July 20, 1997
accepted July 30, 1997.)